Chapters 7 to 10 of

SUPERCONDUCTING COPLANAR DELAY LINES

by

YI WANG

A thesis submitted to
The University of Birmingham
for the degree of
DOCTOR OF PHILOSOPHY

Electronic, Electrical and Computer Engineering
School of Engineering
The University of Birmingham
February 2005

Chapter 7 Fabrication, packaging and measurement set-up

The delay lines are fabricated by patterning the designed layouts in Figure 7.1 into HTS films. For a simple structure, the layout could be drawn directly using the commercial simulation package, such as Sonnet or ADS. However for a complex structure as the double-spiral meander line used here, a special computer programme has to be written to produce the coordinates of every vertex, which are imported into ADS and converted to the layout. This layout is then used by a specialist manufacturer to produce a photomask on a chrome plated glass plate. A positive[*] photomask is used in this work to reproduce the mask pattern on the YBCO film.

7.1 Photolithographic patterning

Both CPW and CBCPW delay lines are patterned with $YBa_2Cu_3O_{7-\delta}$ (YBCO) film on a $LaAlO_3$ (LAO) substrate by photolithography and ion-beam milling. The substrates are double-sided polished with a diameter of 2-inch and thickness of 0.508 mm. The nominal dielectric constant is 23.6. The substrates used for the CBCPW device have YBCO films deposited on both sides, whereas the substrates for the CPW device have YBCO deposited only on one side. The films are 600 nm thick and coated with 50 nm thick gold. This gold layer is used to improve the electrical contact between superconductors and normal conductors, such as the box (ground), coaxial pins of the feeding connectors, or bonding wires.

For the surface containing the YBCO circuit, the patterning process involves two stages and needs two masks, Figure 7.1(a) and (b), to pattern the delay line structure first, and then to make the gold contacts.

In the first stage, both the YBCO and gold layers are etched through to form the pattern of the delay line. Firstly, photoresist (Clariant AZ5214E) is spun onto a cleaned wafer and baked at 105°C for 2 minutes. After aligning with the photomask in a mask-aligner (Karl Suss MJB3), the wafer is exposed to UV light. The exposed photoresist is then dissolved in developer (Clariant AZ527). An ion-beam milling machine (Millatron by Commonwealth

---

[*] A negative mask is used to reproduce the inverse of the mask pattern.

Scientific Corps.) is used to etch the YBCO and gold that is not protected by photoresist, and leave the pattern of the device. A mass spectrometer (Hiden Analytical) is used to detect which ions are being sputtered. This allows to see when the layers are etched through. The remaining photoresist is removed using acetone. After the first stage of patterning, the obtained YBCO circuit is completely covered with a layer of gold.

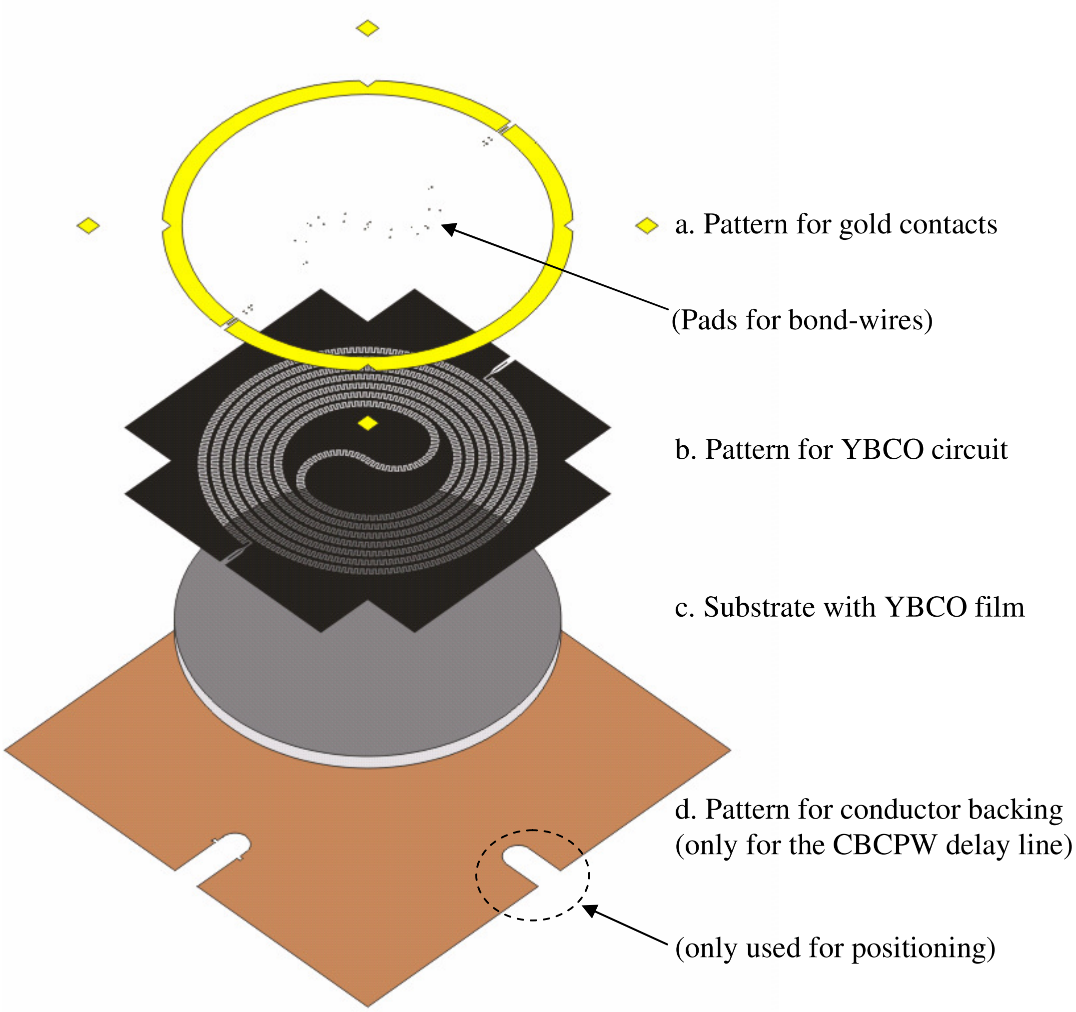

Figure 7.1 The positive masks used in the patterning process, which reproduce their layouts on the YBCO films.

The second stage is to remove most of the gold covering, while leaving the gold pads and strips specified by the pattern in Figure 7.1(a). Photoresist is again spun onto the wafer. Using the mask Figure 7.1(a), a similar process as the first stage follows. Only the gold layer is etched through this time. After clearing the photoresist, a YBCO delay line with gold contacts is completed. A microscopic view of a small area of the finished delay line is shown in Figure 7.2.

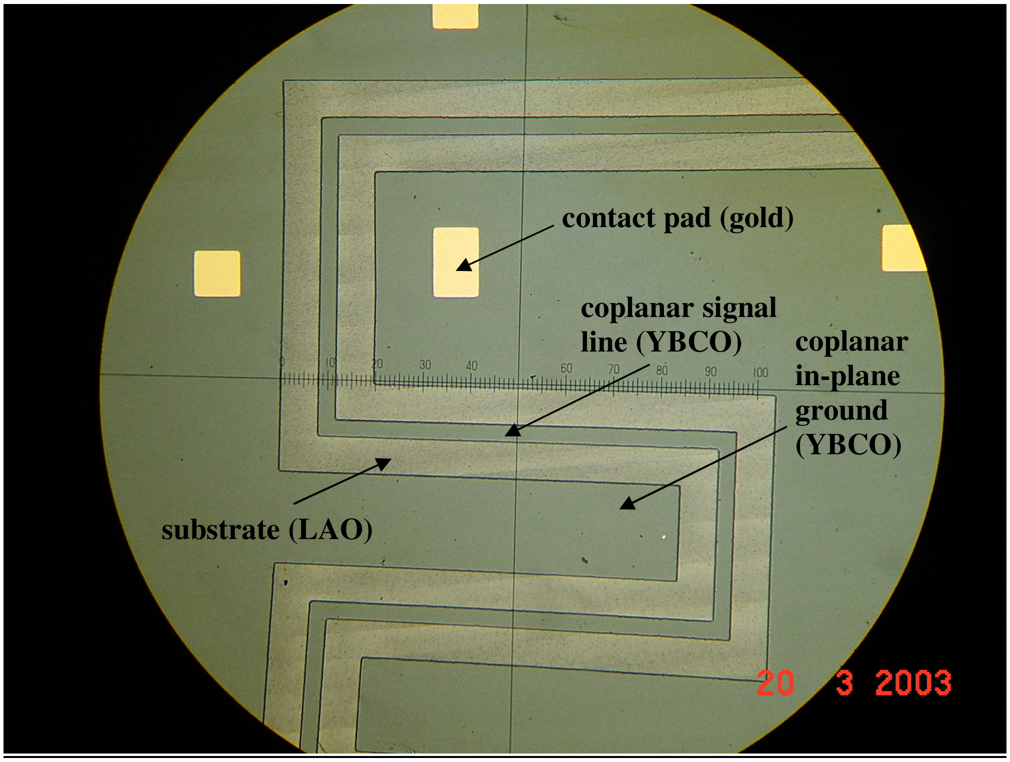

Figure 7.2 Microscopic view of a small area of the finished CBCPW delay line (near the feed-line). The smallest division on the ruler is 10 μm.

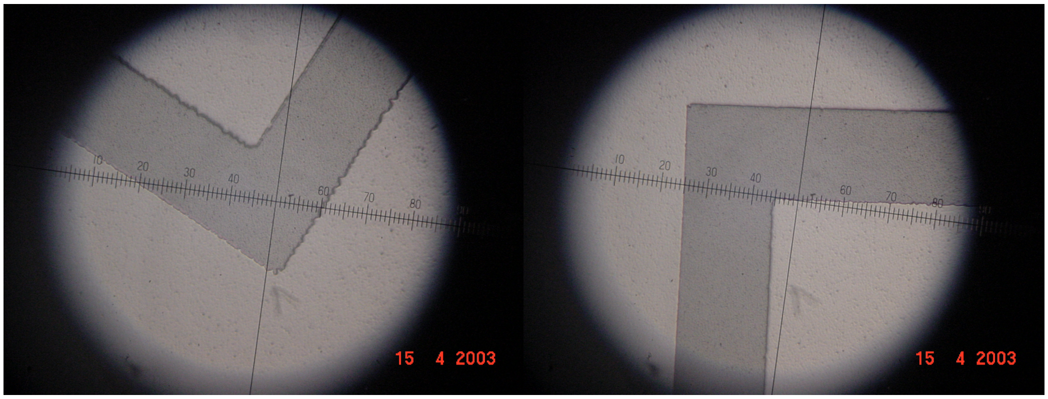

(a) Bad (b) Good

Figure 7.3 Patterned YBCO transmission lines with different qualities on the wafer of the CPW delay line. The smallest division on the ruler is 2 μm.

There have been difficulties in the patterning process raised by the presence of big particles (>0.025mm) on the films with 200nm gold layer. As shown in Figure 7.4, many are comparable to or even larger than the smallest features of the circuits (0.040 mm wide strip or 0.074 mm wide slot). They are gold residues left from the deposition process. The manufacturer was able to get rid of them only by depositing thinner gold. This is why 50nm gold layers are used on my films. However, the wafer still needs to be carefully oriented against the mask to prevent some smaller particles from cutting through the strip or bridging the slot. Otherwise, a single particle may open or short the entire circuit. The large wafer size (2-inch) also presents some problems with the uniformity of the patterned circuit. It is found that the quality of the YBCO trace is different across the wafer as shown in Figure 7.3(a) and (b). The fuzzy edge in Figure 7.3(a) may be due to over-developing. A microscopic examination shows that the transmission line is over-etched by 1-2 μm on the edge, so the average line width would be 0.036-0.038 mm rather than 0.04 mm, and the average slot width is 0.076-0.078 mm rather than 0.074 mm.

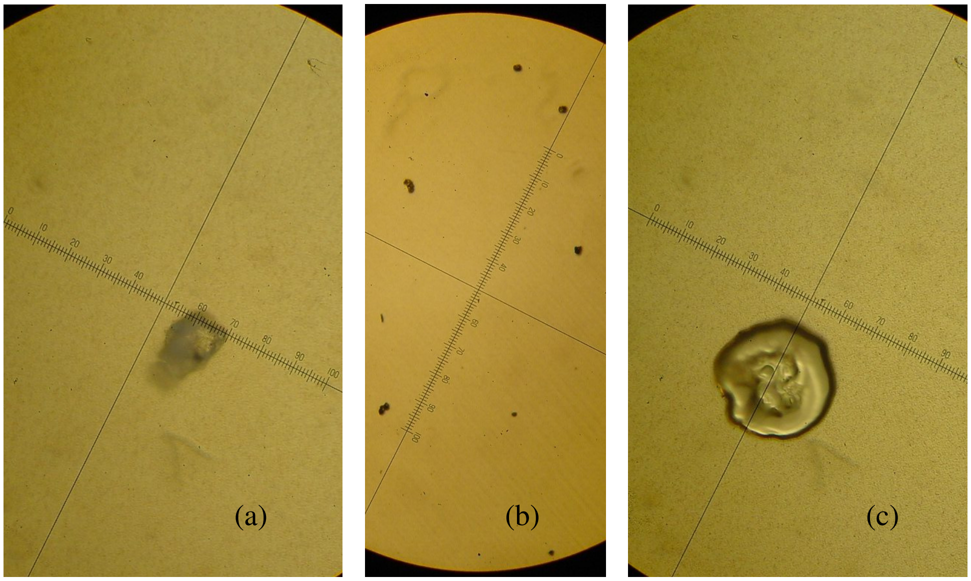

Figure 7.4 Some particles or spots found on the wafers before patterning. The smallest division is 2 μm in (a) and (c), and 10 μm in (b).

For the CBCPW delay line, one more patterning process is needed on the conductor backing. This is to remove the small area of YBCO and gold beneath the taper transitions at the input and output, in order to realize an unbacked CPW taper in the CBCPW delay line. This has been discussed in Chapter 6. As high accuracy is not necessary for this patterning, a copper mask as shown in Figure 7.1(d) is used, and only simple alignment is needed. A mark is firstly put on the wafer edge of the patterned circuit side. As the edge is transparent, we are able to align with the mark when patterning the opposite side. Being seated on the stage of the milling machine, the patterned circuit has to be protected by a thick layer of photoresist, and stuck only against four corners, so as to prevent damages by scratch and excess heat.

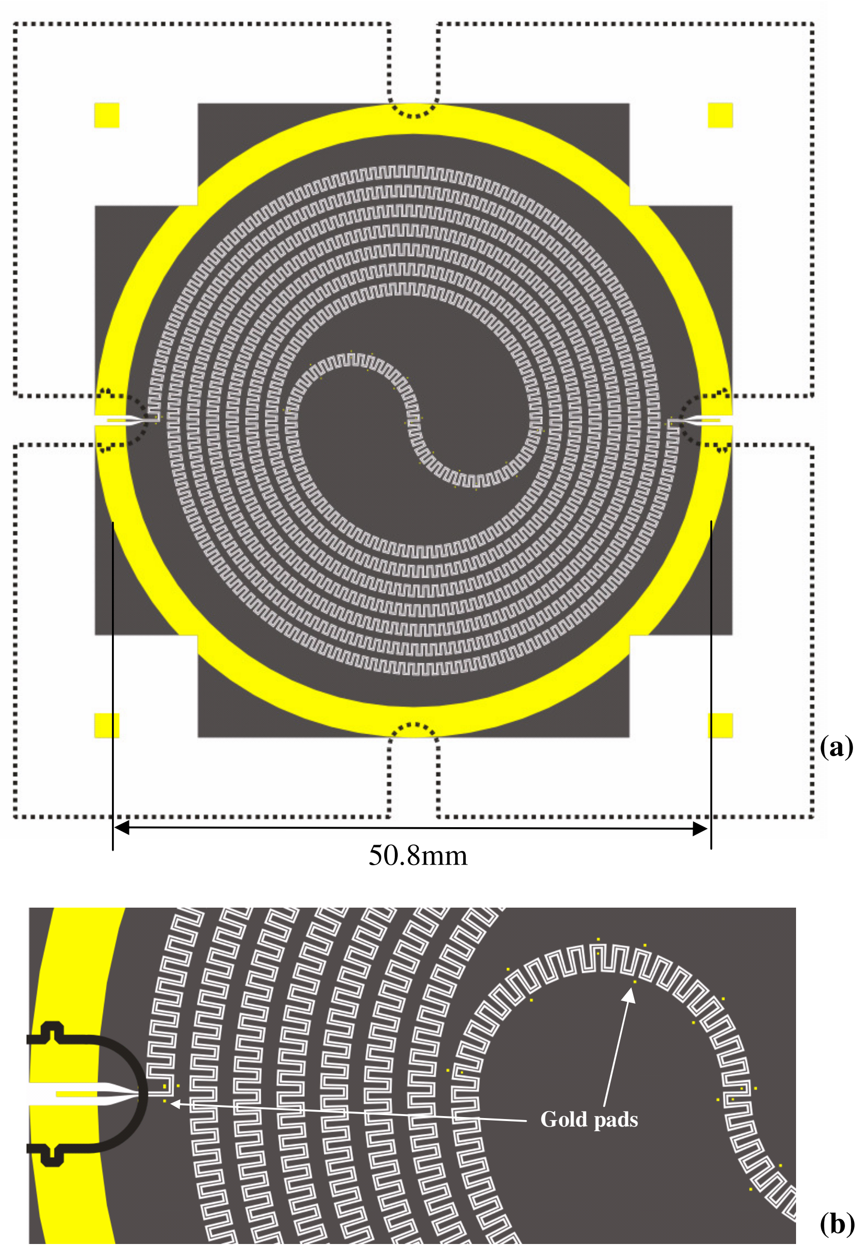

Figure 7.5 (a) Layouts patterned on the YBCO films. (b) An enlarged view of the gold pads for the bond-wires.

The arrangement of overlapping masks shown in Figure 7.5 also gives a visual effect of the patterned circuit. The dark grey area is YBCO film, the yellow area is the gold contact and the dotted line shows the profile of the conductor backing only for the CBCPW delay line. Initially, no crossover wires are bonded on the coplanar circuits of both devices.

7.2 Packaging

Titanium boxes are used to house the circuits, providing a matched thermal expansion with the $LaAlO_3$ substrate. To reduce the conductor loss of the metal walls, the boxes are electroplated with 3 μm gold.

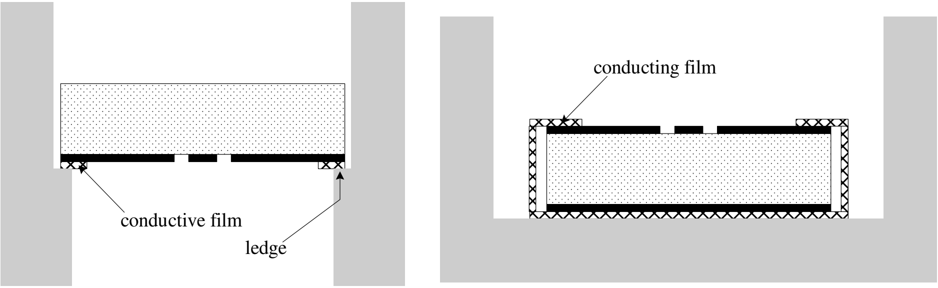

(a) CPW (b) CBCPW

Figure 7.6 The use of conducting adhesive-film to mount the wafer in the metal box.

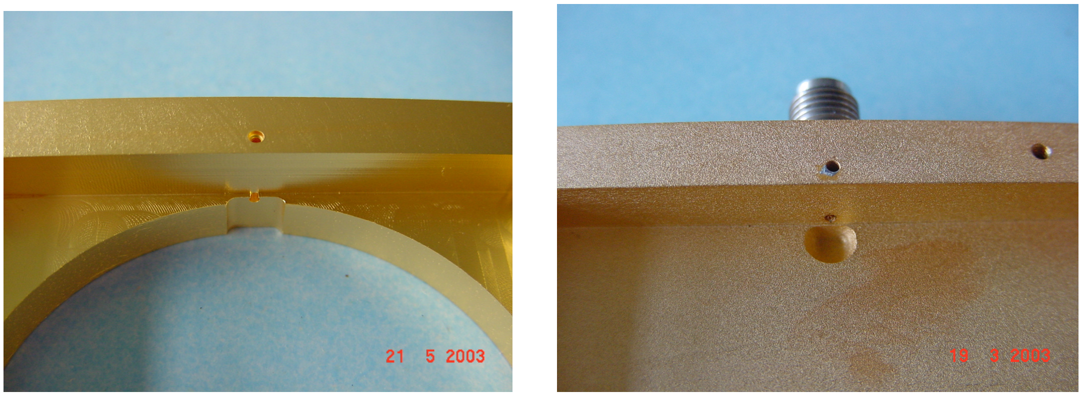

(a) CPW (b) CBCPW

Figure 7.7 The box configurations in the feed-line areas for (a) the CPW delay line and (b) the CBCPW delay line.

The wafer holding the CPW delay line is mounted in the middle of the box with cavities both above and below the wafer and the YBCO circuit face down as illustrated in Figure 7.6(a). The in-plane ground is connected to the box wall by gluing the substrate with electrically-conducting adhesive-film (Ablefilm Adhesive film 5025E) against a 1.0 mm wide ledge. The electrical contact is all along the gold strip shown in Figure 7.5(a). The ledge and the feed-line area in the box are shown in Figure 7.7(a). Beryllium-copper springs (commonly used in other work) are not used to clamp the circuits, in order to avoid the possible resonance modes parasitic in the wide operation band. The package shows good mechanical strength with no deterioration during more than 25 runs of cryogenic microwave measurements.

Unlike the package of the CPW delay line, the wafer holding the CBCPW delay line is directly glued onto the box base, where a recess is bored at the feed-line area as shown in Figure 7.7(b) to make a cavity beneath the taper transition of the delay line. Thus a CPW-type taper can be realized for the CBCPW delay line as discussed in Section 6.3.2. The electrical contact between the conductor backing of the delay line and the box base is again through conducting adhesive-film, which is then wrapped around attaching to the in-plane grounds all along the gold strip, as illustrated in Figure 7.6(b). In this way, the upper and lower ground planes are joined, which is a conventional requirement to reduce the parallel plate modes. To achieve a good contact, continuous pressure needs to be applied to the adhesive film during its cure cycle. However, this is not possible for the wrapped portion. Only point pressure was given to ensure attaching. The electrical contact therefore may not be optimal in this case.

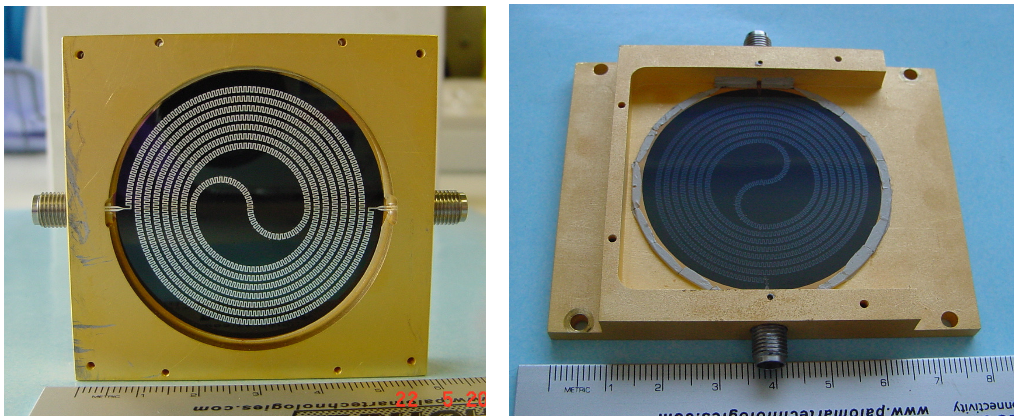

(a) CPW (b) CBCPW

Figure 7.8 Pictures of the packaged (a) CPW delay line and (b) CBCPW delay line.

K-connectors with stress-release sliding contacts are fitted for the input and output connections. The tab of the sliding contact is connected to the central conductor of the coplanar waveguide with silver-loaded epoxy (EpoTek H20E). Alongside of this connection point, the contacts between the in-plane grounds and box wall are also reinforced by epoxy. To achieve an optimal performance, good interconnections both for the signal lines and for the grounds are needed and spurious inductance or capacitance at the connection points should be minimized. The packaged devices are shown in Figure 7.8. In the operation state, the device on the left is closed in with a metal lid and a base. For the device on the right, one of the side-walls is removed to facilitate fitting the wafer. A L-shaped lid is used to enclose the circuit completely.

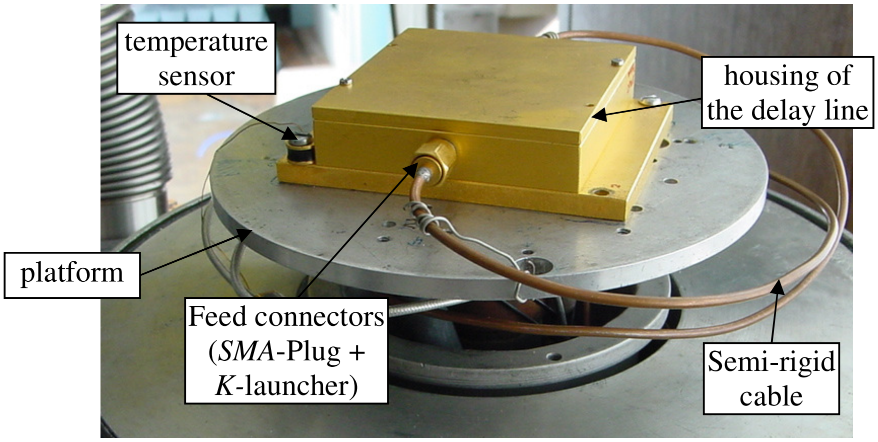

Figure 7.9 Mounting of the delay lines in the cryostat.

7.3 General measurement set-up

As shown in Figure 7.9, the housing of the delay line is mounted on an aluminium platform, which is tightly screwed on the coldhead of a Leybold cryostat. Two diode-temperature-sensors (LakeShore DT-470-DI-13) are used to monitor the temperature of the device, one tightened to the box base and the other to the coldhead. The temperature is stabilized by a controller (Leybold LTC60 or Scientific Instruments 9650). An Agilent 8722ES vector network analyser (50 MHz – 40 GHz) is used to measure S-parameters and time-domain responses of the delay lines. The source power of the network analyser is -10dBm unless otherwise stated. The semi-rigid cable is RG405 as specified by Table D-1 in Appendix D.

Due to the change of the cable attenuation with temperature, room-temperature calibrations cannot be directly used for accurate low-temperature measurements. As shown in Figure 7.10, the measurement system calibrated at room temperature exhibits positive S_{21} when cooled down to 77K. Experiments show that the measured S_{21} differs by 0.2 dB at 0.05 GHz, 0.5 dB at 2 GHz, 1.3 dB at 10 GHz, and 1.9 dB at 18 GHz between room-temperature and 30K calibrations. From 30K to 77K, the difference is only less than 0.1 dB at 18 GHz.

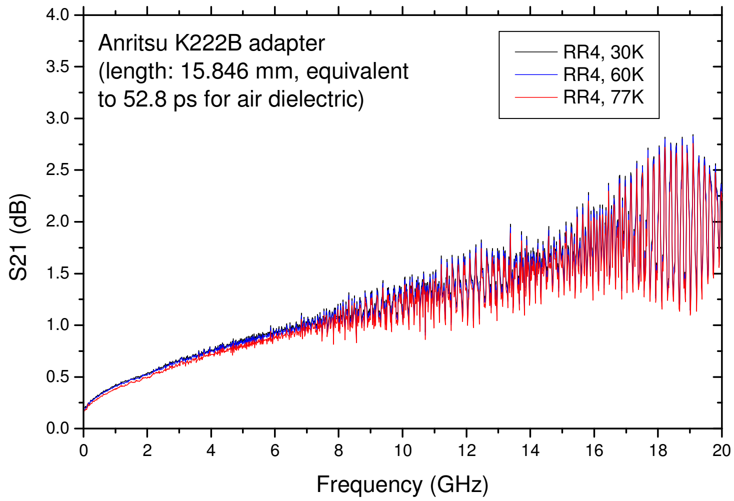

Figure 7.10 Measured S_{21} of an Anritsu K222B adaptor at 30K, 60K, and 77K, with calibrations performed at room temperature using HP 85052B-3.5 mm Calibration Standards.

In this work, direct low-temperature calibrations are performed at 30K, 60K, and 77K for which the measurements are taken, rather than correcting the measurement results based on room-temperature calibration. Separated cooling cycles are involved for the calibrations and the measurements. Since the superconducting temperature could permanently damage the calibration standards (HP 85052B-3.5mm Calibration Kit[†]), a K-type adaptor (Anritsu K222B) is adopted for the response calibration of S_{21}, and a SMA-short (Hubner-Suhner) is used for the response calibrations of S_{11} and S_{22}.

As electrical delays are introduced by these non-standard kits, there would be some errors without compensation. The nominal electrical length of the adaptor is 15.846 mm[‡] with an estimated delay of 0.0528 ns assuming an air dielectric. Measurement shows the electrical delay is 0.0545 ns. To compensate for this, the offset-delay in the definition of the calibration-thru is modified[§] to be 0.0545 ns. The measured insertion loss of the adaptor is less than 0.1 dB up to 20 GHz. As for the SMA-short, an electrical delay (one way transit time) of 0.024 ns is observed from the time-domain reflection response, based on a full 2-port calibration at room temperature. In the calibrations for S_{11} and S_{22}, the definition of the HP 85052B calibration-short is used, with a specified offset delay of 0.0318 ns[†] (0.032 ns by measurement), so a correction of 0.008 ns is needed to compensate for its difference with the

---

[†] User's and Service Guide, Agilent Technologies 85052B, 3.5 mm Calibration Kit, January 2002.

[‡] Data provided through the technical support of Anritsu Ltd., UK.

[§] User's Guide of 8719ET/20ET/22ET/19ES/20ES/22ES Network Analyzers, Agilent Technologies, Inc., June 2002.

0.024ns-delay of the SMA-short. This means the corrected time delay in the reflection response will be 0.016 ns less than the experimental readings. This correction has been verified by measuring the standard calibration kits with known electrical delays. Compared with the total delay (~25.5 ns) of the experimental devices, it can be neglected. The effects on the frequency- and time-domain measurements are expected to be insignificant. However, this correction will be taken into account in looking into the time-domain response of the feed line, which may have features in a time span of 0.05 ns. This will be discussed in Section 9.3.2.

In addition, the low-temperature calibration procedure may bring some uncertainty, as it involves two cooling cycles for the calibration and then the measurement. Disconnections and connections inevitably cause some irrepeatable measurement set-up, which may degrade the calibration accuracy. So, the assembly in the cryostat (Figure 7.9) must be kept in a least altered state and the same tightening torque be maintained for the coaxial connections. Experimental experiences show that the reproducibility of the S_{21} measurements of the delay lines is very good up to 18 GHz, with an uncertainty much less than the measured ripples of the devices.

The quality of the cable-assemblies, interconnecting the device with the measurement system, also plays an important role. About 2.8 m cables are used, including two 1m-long flexible cables connecting the analyser to the hermetic adaptors on the wall of cryostat, and two 40cm-long semi-rigid cables (inside the cryostat) connecting to the device under test. By experience, poor quality assemblies (e.g. inappropriately tightened interconnections, or over-bent semi-rigid cables) could invalidate the calibration and add their own contributions to the measured response. By maintaining steady performance of quality assemblies, calibrations can normally eliminate their effects on the measurement results, and reasonable agreement between different runs of cryogenic measurements can be achieved.

Chapter 8 Characterisation of Delay Lines using Resonator Techniques

8.1 Introduction

Although delay lines in practice operate in a full transmission state, resonator techniques, in which the input and output are only weakly coupled to the transmission line, are effective and informative in characterising the loss level and dispersion. The resonator techniques have the advantage of measuring circuit losses without being affected by the quality of connections at the input/output port. These measurements can then be compared with those from fully connected device. This technique can be adopted to characterise material properties as well, such as the surface resistance of superconductors, which is one of the major concerns in this chapter. A delay line resonator itself may also have applications in radio frequency (RF) filters, oscillators, or frequency standards.

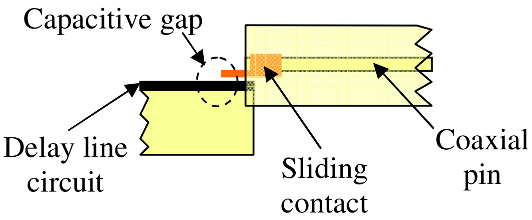

Figure 8.1 Configuration of the capacitive gap used to achieve the external coupling for the delay line resonators.

Both delay lines (CPW and CBCPW) are made into resonators for the first stage of the measurement. As illustrated in Figure 8.1, the external coupling is achieved by not connecting the input and output K-connector pins, but leaving a small capacitive gap between the pin (with the sliding contact) and the coplanar signal line. The delay line resonates when its total length l (l=2.28 m) is an integer number of half-wavelengths. The wavelength λ_n of the n-th harmonic would be (ignoring the fringing effect on the total line length l)

$$\lambda_n = 2 \cdot l/n, \quad n = 1,2,\cdots \qquad \textbf{Equation 8-1}$$

where n is the index of each harmonic and n=1 corresponds to the fundamental mode.

Resonant frequencies and quality factors of more than 1000 harmonics for each resonator (CPW and CBCPW) are acquired from 20 MHz (the fundamental mode) up to 20 GHz. The attenuation coefficients of the delay line and surface resistance (R_s) of the HTS are then evaluated. The frequency-dependence of R_s is investigated over the wide and continuous band. There has not been such a wide band characterisation of superconductors using coplanar resonator techniques. The results reported in this work may be complementary to other scarce measurement data based on resonator techniques[1], where characterisations were taken only at a few frequencies, due to the limitations in resonator size or the ability to accurately measure many modes over a wide frequency range. Some other characterisation methods have been reviewed in Section 3.3.

8.2 Acquisition of Q values as a function of frequency

8.2.1 Quality factors

Quality factor (Q) is an important measure of the loss of a resonant circuit. It is defined as

$$Q = \omega \frac{\text{average energy stored}}{\text{energy dissipation/second}}$$

For a superconducting circuit, the energy is dissipated in the superconductor, in the dielectric substrate, and by radiation. So, if Q_c, Q_d and Q_r are the quality factors of the superconductor, dielectric and radiation respectively, the unloaded quality factor Q_0 of a resonator can be expressed as

$$\frac{1}{Q_0} = \frac{1}{Q_c} + \frac{1}{Q_d} + \frac{1}{Q_r} \qquad \textbf{Equation 8-2}$$

Here Q_0 is an intrinsic value of the resonator itself and different from the measured quality factor, or loaded quality factor Q_L. To be able to measure a resonator, enough energy has to be coupled into the resonator so that the response can be seen. This incurs another loss associated with this external coupling. It can be characterised by an external Q, or Q_e. The loaded quality factor Q_L can be written as

$$\frac{1}{Q_L} = \frac{1}{Q_0} + \frac{1}{Q_e} \qquad \textbf{Equation 8-3}$$

For a symmetrically coupled resonator, where the external Q at the input port equals that at the output, the unloaded quality factor Q_0 can be related to Q_L by the transmission coefficient S_{21} at the resonant frequency f_0. That is

$$Q_0 = \frac{Q_L}{1-\left|S_{21}(f_0)\right|} = \frac{Q_L}{1-10^{IL/20}} \qquad \textbf{Equation 8-4}$$

where *IL* is the transmission loss in dB. If *IL* is less than -20 dB, the resonator can be regarded weakly coupled. This is the case for both resonators measured in this work. It should be noted that the coupling structure of the delay line resonators cannot be ensured to be symmetric due to the way the external coupling has been achieved (Figure 8.1). However, equation (8-4) can still be used, in consideration that the magnitude of S_{21} is much less than 1. A small error in S_{21} would not result in a large inaccuracy of Q_0.

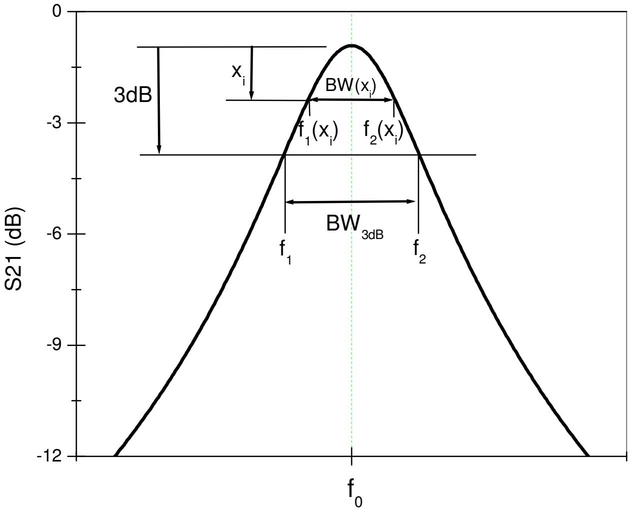

Figure 8.2 Measurement of *Q*-values from the magnitude of transmission coefficient S_{21}.

There are many different methods to measure the Q-values and resonant frequencies of a resonator.[2] In this work, 3dB-method and Lorentzian-curve-fitting-method are used to determine the loaded Q based on the transmission coefficient as a function of frequency.

The 3dB-method is the simplest and fastest way to determine Q. In a transmission coefficient versus frequency curve as illustrated in Figure 8.2, the resonant frequency f_0 is the frequency at the maximum magnitude. The 3dB-Q is given by

$$Q_L = f_0 / BW_{3dB} \qquad \textbf{Equation 8-5}$$

where $BW_{3dB}=f_2-f_1$ is the difference between the two frequencies corresponding to half power points ($1/\sqrt{2}$ of or 3dB) from the maximum of $|S_{21}|$ as shown in Figure 8.2. However, equation (8-5) does not contain much information about the profile of the resonant curve. Its accuracy is poor when the signal-to-noise ratio is low.

A more robust method to evaluate Q is through fitting the $|S_{21}|$ versus f data to a Lorentzian curve, which describes the magnitude of the transmission coefficient in the proximity of the resonant peak as

$$\left|S_{21}(f)\right| = \frac{\left|S_{21}(f_0)\right|}{\sqrt{1+4{Q_L}^2\left(\frac{f}{f_0}-1\right)^2}} . \qquad \textbf{Equation 8-6}$$

A nonlinear least-square fit procedure in the range of $0.8\text{dB} \le x_i \le 3\text{dB}$ (x_i is defined in Figure 8.2) is used to find Q_L from $|S_{21}(f)|$. This method gives much better accuracy than the 3dB-method when the resonant trace is noisy, which happens in this measurement below 1 GHz where the external coupling is extremely weak, and at 77K when the temperature is close to T_c. It should be noted that Lorentzian-method is normally used in the limit of weak coupling and for symmetric resonant curves.

According to our experiments, the 3dB-Q is generally higher than the Lorentzian-Q. They differ by less than 20% for the CPW resonator and 10% for the CBCPW resonator at most of the frequencies from 0.2 to 22 GHz. The difference is particularly big under certain circumstances, such as when the temperature is 77K or the frequency is lower than 1 GHz. Both relate to the increased noise levels.

8.2.2 Data acquisition procedure

An in-house data-acquisition programme (written in National Instruments LabWindows CVI) is adapted from D. W. Huish's work[3] to conduct computer-controlled measurements. New functions are added in the programme to trace and characterise the resonant peaks over the frequency range from 20 MHz to 20 GHz. The temperature controller and network analyser are connected to a PC via GPIB interfaces as diagrammed in Figure 8.3. Unlike transmission measurements, resonant measurements are not very sensitive to the accuracy of calibrations. So, only room-temperature calibrations are performed over a wideband up to 22 GHz. When a subset of the calibrated frequency range is measured, interpolated corrections are used.

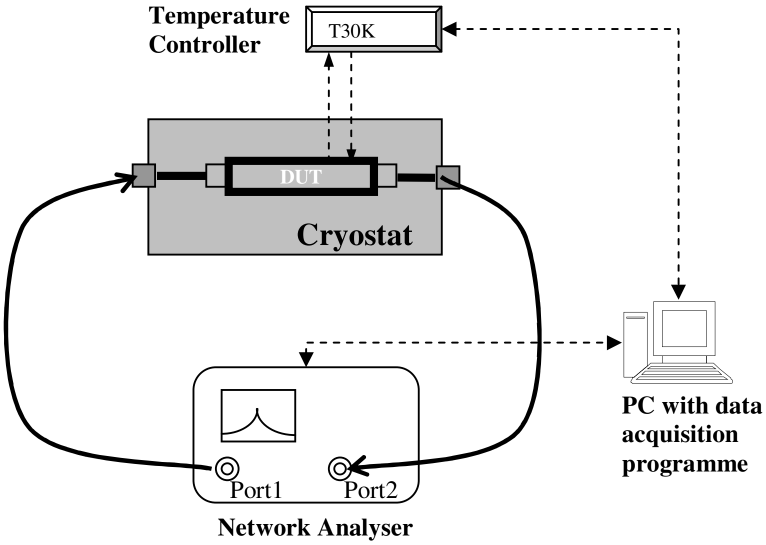

Figure 8.3 Experimental arrangement for the measurement of Q as a function of frequency at different temperatures.

Due to the presence of spurious resonances, it is very difficult to sweep automatically the thousands of harmonics using the available searching functions of the network analyser. Hence, a semi-automatic approach is adopted to locate and characterise each harmonic.

To begin with, let Δf be the frequency difference between a pair of adjacent harmonics. Δf, as a function of resonant frequency, can be pre-determined approximately by fitting the data acquired manually at few frequencies. The fit function $\Delta f(f)$ is then embedded into the data-acquisition programme as a control scheme for an automatic harmonic sweep. If necessary, this $\Delta f(f)$ can be refined by fitting more or the entire data after the first sweep.

By experience, however, a fit function based on several data points would be sufficient for an effective sweep over the wide band of interest.

The tracing of each harmonic is then accomplished by sequentially setting the sweep range of the network analyser centred at $f_i = f_{i-1} + \Delta f(f_{i-1})$ with a span of $\Delta f(f_{i-1})$, which is controlled by the data acquisition programme. Once a single resonance is displayed on the monitor of the network analyser, a series of computer-controlled measurements follow. These include the resonant frequency, 3-dB bandwidth, S_{21} at the resonant frequency, 3dB-*Q*, and Lorentzian-*Q*. Also acquired are the index of each harmonic, and a factor Δf_{cent} characterising the skew of resonance curve, which will be detailed in Section 8.4.

As an example, a polynomial fit of Δf for the CPW delay line resonator at 30 K is shown in Figure 8.4.

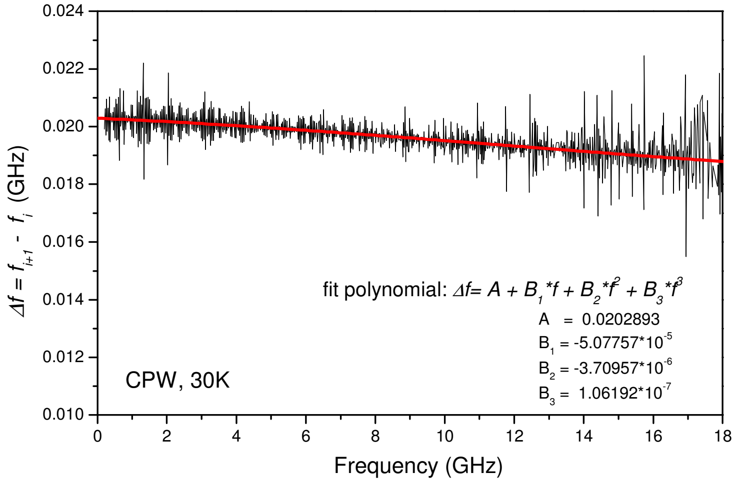

Figure 8.4 The difference ($\Delta f = f_{i+1} - f_i$) of the resonant frequencies between each pair of adjacent harmonics, and the polynomial fit function $\Delta f(f)$ for the CPW delay line resonator at 30K.

8.2.3 Measurement results

8.2.3.1 Fundamental mode

The fundamental (lowest) resonant frequency at 30 K is 20.2540 MHz for the CPW delay line resonator (Figure 8.5) and 20.0458 MHz for the CBCPW, with quality factors of 28140 and 32608 respectively. The small difference in the fundamental resonant frequencies indicates a slightly larger effective permittivity of the conductor-backed coplanar waveguide.

The bigger Q-value of the fundamental mode in the CBCPW resonator is not expected and this is contrary to a general profile of lower Q-values for the CBCPW resonator over the wide frequency range.

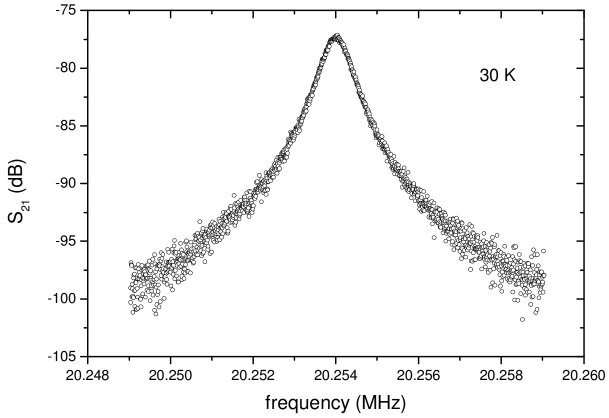

Figure 8.5 Fundamental (lowest) resonance for the CPW delay line resonator at 30K.

Because the fundamental mode is beyond the lower frequency limit (50MHz) of the Agilent 8722ES network analyser, an Anritsu MS4623 network analyser (10MHz-6GHz) is used to cover. According to our measurements, MS4623 shows better noise figure below 0.2 GHz. This results in lower Q-values than those measured by 8722ES. Above 0.2 GHz, the measurements from both analysers agree well with each other.

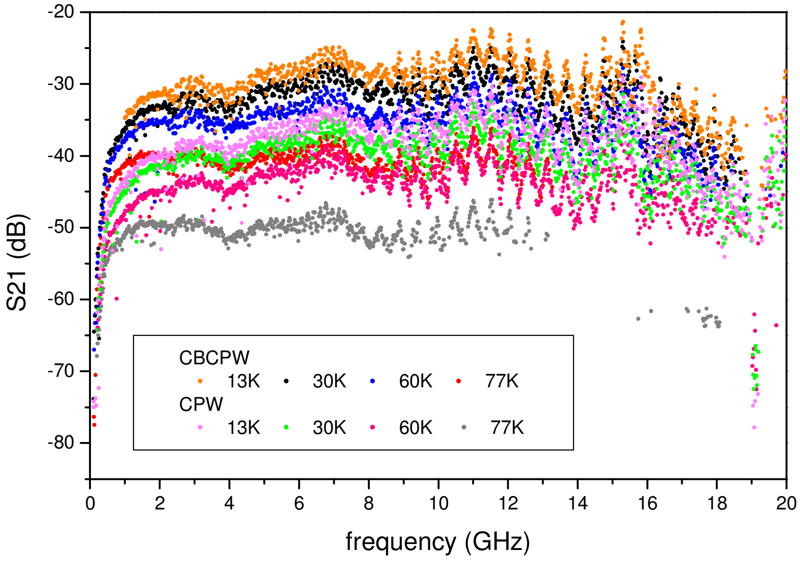

Figure 8.6 Measured S_{21} at the resonant frequencies of the harmonics.

8.2.3.2 *Q* values as a function of frequency

Figure 8.6 shows the measured S_{21} at the resonant frequency of each harmonic. The insertion loss is markedly large below 1 GHz due to the extremely weak external coupling, and at 77K due to the rapidly increasing surface resistance as the temperature approaches the superconducting transition. The analogous profiles of the overall responses in Figure 8.6 between CPW and CBCPW indicate a similar coupling structure. But the magnitude of the external coupling in the CPW resonator is lower, resulting in a smaller S_{21}.

The unloaded *Q* values as a function of frequency are shown in Figure 8.7 for the CBCPW line resonator and Figure 8.8 for the CPW resonator. Experiments show that the difference between Q_0 and Q_L is less than 0.5% at 77K, 3% at 30K for the CPW resonator, and 2% at 77K, 6% at 30K for the CBCPW resonator. At 77 K, the harmonics above 13 GHz are too lossy to be characterised. At 30K and 60K, the harmonics are characterisable up to 20 GHz, but no regular resonant peaks can be observed at around 19 GHz. The S_{21}-graphs in Figure 8.6 also break at 19 GHz. This frequency corresponds to the bandgap predicted by the full-wave simulations in Figure 5.7. As expected, the *Q*-values decrease with increasing frequency and temperature.

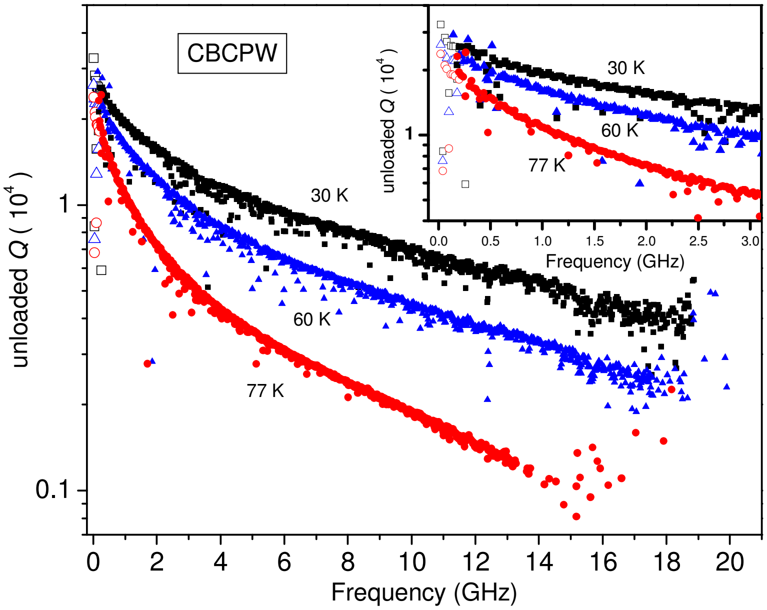

Figure 8.7 Unloaded *Q*-values as a function of frequency for the CBCPW delay line resonator. The *Q*-values below 0.2 GHz are measured by Anritsu MS4623 network analyser.

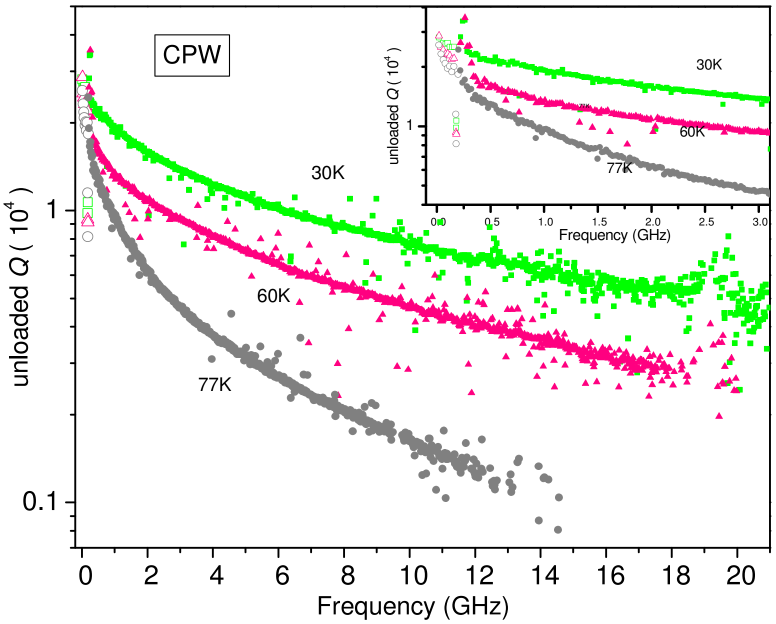

Figure 8.8 Unloaded *Q*-values as a function of frequency for the CPW delay line resonator. The *Q*-values below 0.2 GHz are measured by Anritsu MS4623 network analyser.

8.2.3.3 Effect of spurious modes

Mode interference/conversion may significantly affect the resonances, which manifest themselves as anomalous scatter of points in the *Q*-values of Figure 8.7 and Figure 8.8. Interestingly, the *Q*-*f* graphs for the CPW and CBCPW exhibit distinct anomalies: the graphs for the CPW resonator have anomalous points both below and above the general curves of *Q*, whereas the graphs for the CBCPW resonator only have anomalous dips below the general curves. Two typical resonant curves with anomalous *Q* (dips) in the CBCPW resonator are shown in Figure 8.9, both with unexpectedly lower S_{21} than adjacent harmonics. The excessive loss in the case of Figure 8.9(b) is caused by package modes which will be discussed later in more detail, whereas in Figure 8.9(a) the reason is still indefinite. Unlike the CBCPW, the harmonics of the CPW resonator with anomalous *Q*-values are mostly split into two peaks as shown in Figure 8.10. Looking into the change of the split resonances with temperature may help understand their characteristics. In Figure 8.10(a), the resonance around 1.335 GHz splits at all three temperatures (13, 30, and 60 K). Note that these three resonances at different temperatures are the same order of harmonics, i.e. they have the same index. This is different from the case in Figure 8.10(b). At ~6 GHz, the shift of resonant frequency as temperature increases from 13K to 30K is only 2.9 MHz, whereas the shift between 30K and 60 K is 18 MHz, comparable to the frequency difference (~20 MHz) between adjacent harmonics. Therefore, although the three resonances at the three temperatures appear to be at similar frequency, the resonance at 13K and 30K is not the same order of harmonic as the one at 60K. Correspondingly, it can be seen that the resonance peak only splits at 13K and 30K but not at 60K. This implies that the split is more likely due to parasitic modes accompanying the dominant CPW-mode harmonics, rather than those which are insensitive to temperatures, such as the package modes or the modes from the substrate. The parasitic modes could be slotline modes, which interfere with the coplanar modes and split the resonant peaks.

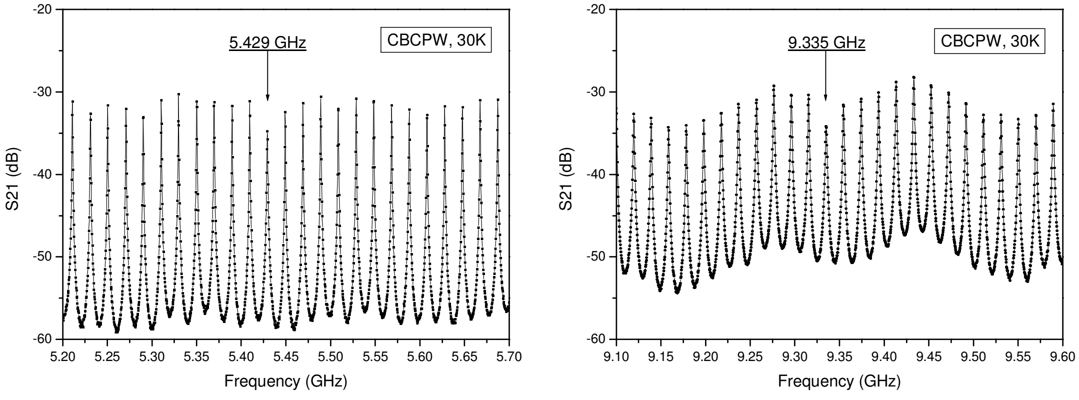

(a) (b)

Figure 8.9 Two typical measured resonant curves corresponding to the dips in the *Q-f* graph of the CBCPW delay line resonator.

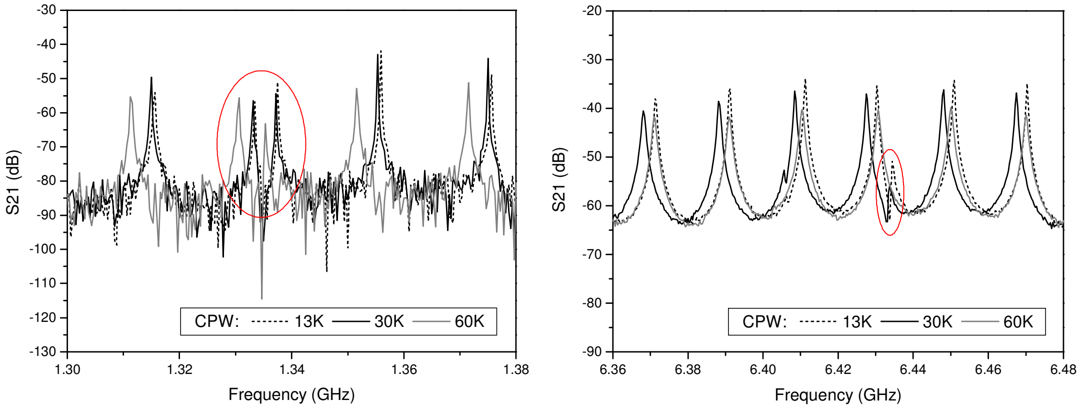

(a) (b)

Figure 8.10 Two typical measured resonant curves corresponding to the anomalous points in the *Q-f* graph of the CPW delay line resonator.

By removing the box lids of the devices, the effect of radiation is examined. (Note that the device is still enclosed by a cryostat, with a cylindrical cavity of 30 cm high and 20 cm in diameter.) It is found that both resonators have negligible radiation loss. The measured *Q*-values of the CBCPW resonator before and after removing the box lid are compared in Figure 8.11. The removal of the box lid (in this device, this also leaves one of the side-walls open [see Figure 7.8b].) should eliminate the possible package resonant modes. This is proven by the fact that when the lid is removed, some anomalous dips disappear at those frequencies where the package modes occur, as can be seen from Figure 8.11. This includes the 9.335 GHz resonance shown in Figure 8.9(b). However, the rest of the dips are almost unaffected. The unaffected anomalies, including the case in Figure 8.9(a), may be related to parallel-plate modes, which can be established between the upper and lower ground planes of the CBCPW structure. There are few dips emerging after removing the lid, which may be due to the radiation loss.

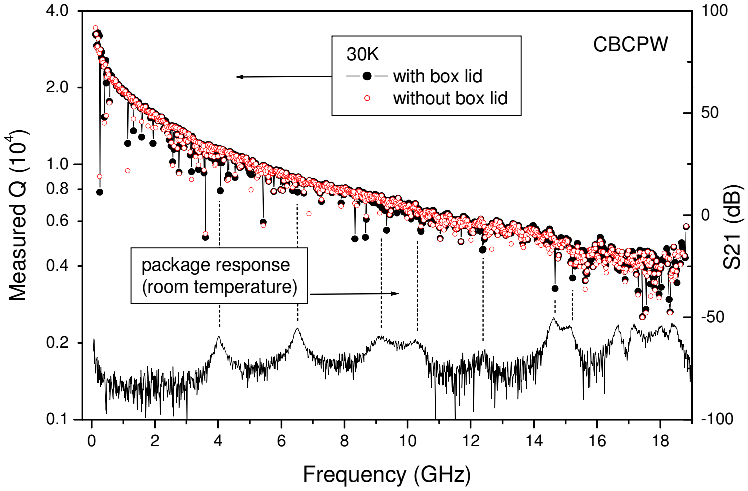

Figure 8.11 Comparison of the measured *Q*-values of the CBCPW resonator before and after removing the box lid. Also included is the package response measured at room temperature when there is neither resonance nor transmission on the superconductor CBCPW circuit.

8.2.4 Estimation of experimental errors

In this work, the characterisation is taken over a wide frequency band to make it useful to study the frequency-dependent properties of the HTS. For this purpose, the frequency-dependence of the *Q*-values is of more importance than the absolute value, therefore the error analysis will focus on the sources of experimental errors, which are sensitive to frequency.

Firstly, the noise present in the resonance curve causes inaccuracy in measuring S_{21}. It is more of a problem at below 0.2 GHz, as the signal-to-noise ratio is so poor due to the extremely low external coupling. This brings uncertainty to the bandwidth BW (Figure 8.2) and affects the Q-value. The relative error of 3dB-Q caused by the uncertainty ΔS in measuring S_{21} can be found as[4]

$$\left|\frac{\Delta Q_L}{Q_L}\right| = \left|\frac{\Delta BW}{BW}\right| = 0.23 \cdot \Delta S \qquad \textbf{Equation 8-7}$$

$$\left|\frac{\Delta Q_0}{Q_0}\right| = \sqrt{\left(\frac{\Delta BW}{BW}\right)^2 + C^2 (\Delta S)^2} = \sqrt{0.053 + C^2} \cdot \Delta S \qquad \textbf{Equation 8-8}$$

where, $C = \left|\frac{\ln 10}{20} \frac{10^{S_{21}/20}}{1 - 10^{S_{21}/20}}\right|$,

assuming the reading of f_0 is accurate. According to Figure 8.6, S_{21} is lower than -20 dB, so the multiplicative factor C is less than 0.013 and the contribution of C^2 in (8-8) is negligible. Hence

$$\left|\frac{\Delta Q_0}{Q_0}\right| \approx \left|\frac{\Delta Q_L}{Q_L}\right| = 0.23 \cdot \Delta S \qquad \textbf{Equation 8-9}$$

This is the case for a weakly coupled resonator.

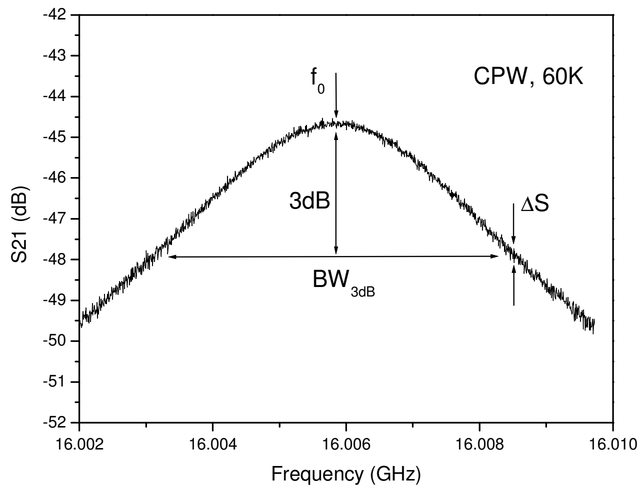

Figure 8.12 Definition of the uncertainty ΔS of the measured S_{21} due to the noise present in resonance curves.

The uncertainty ΔS due to noise is defined in Figure 8.12. These uncertainties observed in the measurement of the CPW resonator are listed in Table 8-1. The largest ΔS occurs below 0.2 GHz. Even with reduced IF bandwidth (300Hz) and with the trace averaging activated in the network analyser, the resonance curves in this region are still noisy due to extremely low S_{21}, which is less than -50 dB. The relative errors estimated by (8-9) are also tabulated. Using the Lorentzian method to acquire Q can reduce the effect of noise. However, because it also relies on S_{21} measurements, the large uncertainty at below 0.2 GHz still presents problem. Therefore, it is believed that Q-values are subject to small overestimation at the low frequency end.

Table 8-1 The relative error caused by the noise in measuring *Q*-values of the CPW delay line resonator.

T (K)	f_0 (GHz)	ΔS (dB)	$\lvert \Delta Q_L / Q_L \rvert$
60	< 0.2	1.0	23.0%
	<2.0	0.2	4.6%
	<10	0.1	2.3%
	<16	0.2	4.6%
	<18	0.4	9.2%

It is also important to note another measurement error due to the superposition of adjacent resonances especially at high frequencies. As the frequency goes higher, the difference ($S_{P\text{-}V}$, marked in Figure 8.13(a)) between the peak and valley of each resonant curve is reduced due to increased insertion loss and decreased Q. Above 10 GHz, $S_{P\text{-}V}$ is less than 20 dB. The superposition between adjacent harmonics becomes important, which may affect the bandwidth of the resonance and then the quality factor. The misestimation can be approximately quantified in the following simplified procedure.

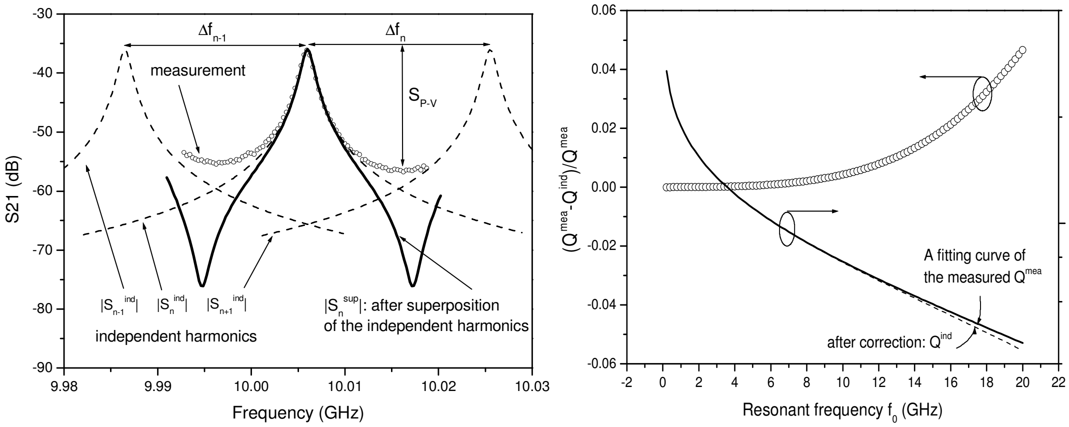

(a) (b)

Figure 8.13 (a) Illustration of the superposition between adjacent harmonics. Only the magnitudes of the transmission coefficients are shown. (b) Estimated error of *Q*-values caused by the superposition in the CPW delay line resonator at 30K. Q^{mea} is the measured value, and Q^{ind} is the corrected value of the independent harmonic before superposing with adjacent harmonics, extracted by using (8-10).

If the measured complex transmission coefficient S_{21} of the *n*-th harmonic can be regarded as a superposition of three independent harmonics of Lorentzian-type as shown in Figure 8.13(a), one has

$$\begin{aligned} S_n^{\sup}(f) &= S_{n-1}^{ind} + S_n^{ind} + S_{n+1}^{ind} \\ &= \frac{S_{n-1}}{1 + j\dfrac{(w_n + 2\cdot\Delta f_{n-1})}{BW_{n-1}}} + \frac{S_n}{1 + j\dfrac{w_n}{BW_n}} + \frac{S_{n+1}}{1 + j\dfrac{(w_n - 2\cdot\Delta f_n)}{BW_n}} \end{aligned} \qquad \textbf{Equation 8-10}$$

where $\Delta f_n = f_{n+1} - f_n$ (~0.02 GHz) as in Figure 8.4, $w_n = 2(f - f_n)$, and S_{n-1}, S_n, S_{n+1} are the maximum transmission coefficients at the resonant peaks. As Δf_n is much smaller than most of the resonant frequencies of interest, it is a good approximation to assume $\Delta f_{n-1} = \Delta f_n$, $S_{n-1} = S_n = S_{n+1}$, and $BW_{n-1} = BW_n = BW_{n+1}$. Hence, $S_n^{\sup}(f)$ can be simplified as a superposition of three harmonics with similar shape but different phases, giving

$$\begin{aligned} S_n^{\sup}(f) &= S_{n-1}^{ind} + S_n^{ind} + S_{n+1}^{ind} \\ &= \left[\frac{1}{BW_n + j(w_n + 2\cdot\Delta f_{n-1})} + \frac{1}{BW_n + jw_n} + \frac{1}{BW_n + j(w_n - 2\cdot\Delta f_n)}\right]\cdot S_n \cdot BW_n \end{aligned} \qquad \textbf{Equation 8-11}$$

In (8-11), BW_n is the unknown parameter. It can be found by equating the 3dB-*Q* derived from $\left|S_n^{\sup}(f)\right|$ with the measured value. Then, the corrected quality factor Q_n^{ind} of the independent harmonic before superposition can be obtained by f_n / BW_n.

As shown in Figure 8.13(b), the error in *Q*-values, estimated using the above procedure, is very small, only 3.2% at 18 GHz and less than 0.5% below 10 GHz for the CPW delay line resonator. In Figure 8.13(a), the superposed resonance curve formulated by (8-10) is compared with the measured one around 10 GHz. At the resonance valley, the estimated S_{21} is lower than the measurement, due to the out-of-phase cancellation between adjacent harmonics. However, it should be noted that this does not adequately represent the real situation, as the Lorentzian representation of each independent resonance in equation (8-10) is only valid in the proximity of the resonance peak[5].

Besides the aforementioned two sources of errors which are sensitive to frequency, there are other random errors due to the instrument limitation of the network analyser or the temperature instability. These may affect the absolute values of the measured Q, but have little effect on its frequency-dependence. The effect of temperature instability on the measurement will be discussed in Section 8.3.

8.3 Temperature dependence measurements

The temperature dependences of quality factors and resonant frequencies are measured at 0.2, 2.0 and 10.0 GHz and shown in Figure 8.14 and Figure 8.15. The superconducting transition temperature T_c is about 86 K, estimated from Figure 8.14. Figure 8.15 shows that the fractional frequency shift $\Delta f / f$ does not change with frequency. As discussed in the context of (3-41), this indicates, as expected, the penetration depth of the superconductor is independent of frequency. However, $\Delta f / f$ increases rapidly as the temperature approaches T_c due to the fast changing kinetic inductance. The frequency shifts for the CPW and CBCPW resonators are close to each other from 13 K to 70 K. Only a small deviation occurs above 70 K. Slightly different superconducting transition-temperatures might result in this. At 0.2 GHz, the Q-T graph for the CPW in Figure 8.14 is not well produced due to the poor signal-to-noise ratio of the measurement.

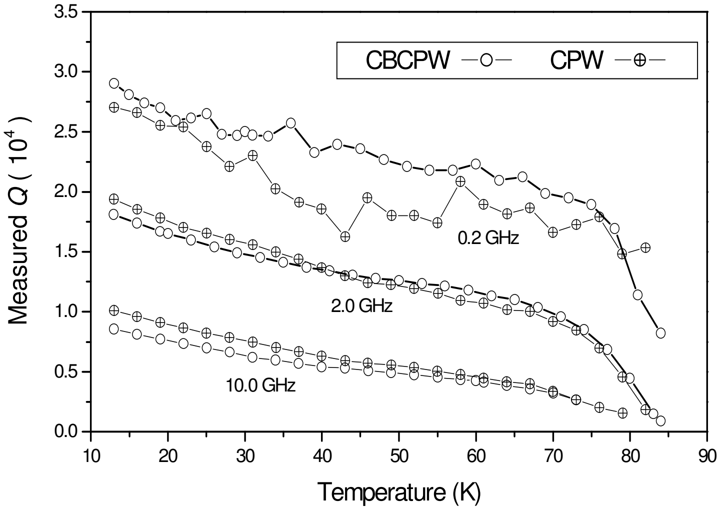

Figure 8.14 The measured temperature-dependent quality factors of the harmonics at 0.2, 2.0 and 10.0 GHz for both the CPW and CBCPW resonators.

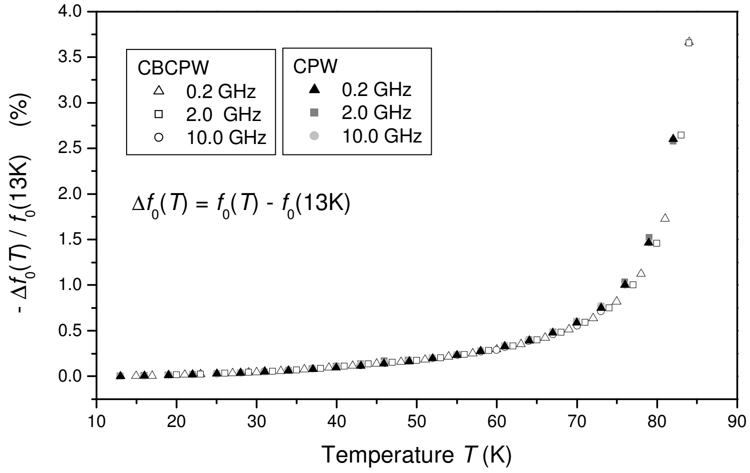

Figure 8.15 The fractional frequency shifts as a function of temperatures for the harmonics at 0.2, 2.0 and 10.0 GHz.

From the temperature-dependence measurement, the experimental uncertainty of Q_L, f_0, and S_{21} due to temperature instability can be estimated. These are given in Figure 8.16 in terms of the percentage errors by 1K variation in temperature. These errors are insensitive to frequency. When the temperature is lower than 60K, the percentage errors are less than $2\%\cdot K^{-1}$ for Q_L, $0.6\%\cdot K^{-1}$ for S_{21}, and $0.02\%\cdot K^{-1}$ for f_0. As the temperature approaches the superconducting transition, these errors increase rapidly. So, the measurement at 77K would have expected more experimental error due to the temperatures instability.

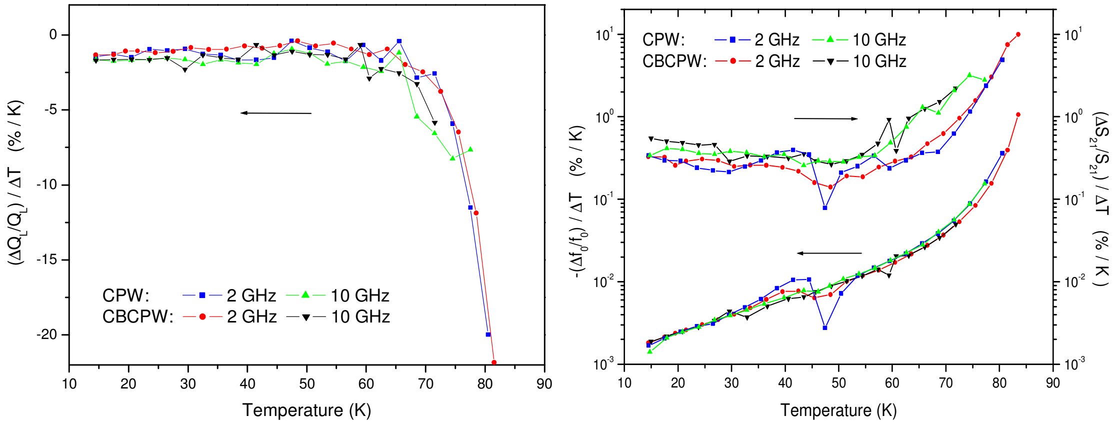

(a) (b)

Figure 8.16 The percentage errors caused by 1K variation of temperature for the measured Q_L, f_0, and S_{21}. These are estimated from the temperature-dependence measurements of the CPW and CBCPW delay line resonators at 2 and 10 GHz.

8.4 Power dependence measurements and nonlinearity

The experimental arrangement of the power-dependence measurement is shown in Figure 8.17. The source power of the network analyser is boosted using a HP83006A amplifier and then fed into the test port of the resonator.

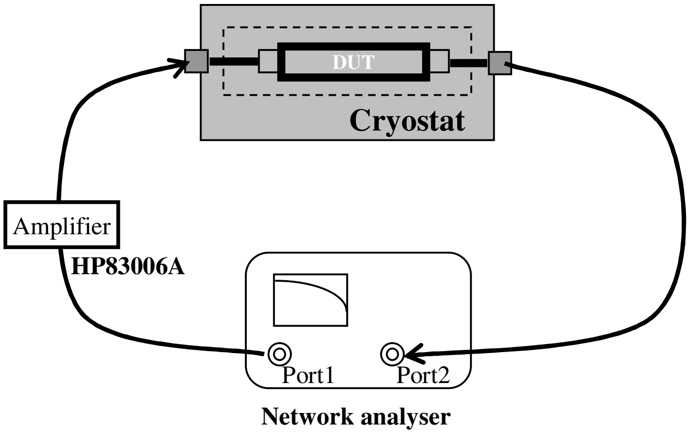

Figure 8.17 Experimental arrangement of the power-dependence measurement. The minimum gain of HP83006A Amplifier is 20 dB. The gain flatness is ± 5 dB at 0.01-5 GHz, and ± 3 dB at 5-26.5 GHz. The power into the test port is not levelled over the frequency range.

Figure 8.18 shows the change of the resonance curve at ~60 MHz as the microwave power to the input port increases. The resonant frequency shifts to lower frequency and the insertion loss increases. All three resonance curves are slightly skewed. A higher input power clearly improves the signal-to-noise ratio.

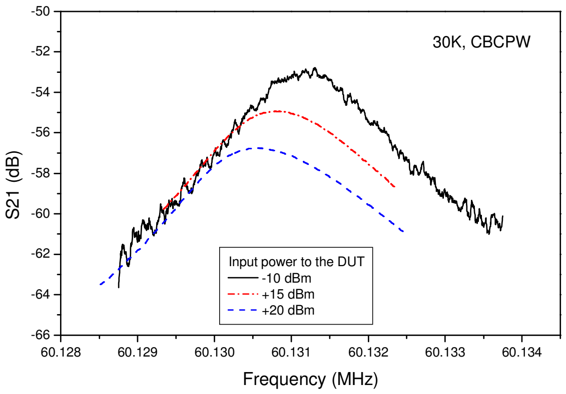

Figure 8.18 Observation of the change of the resonance curves at ~60 MHz with increasing input power to the CBCPW resonator. Note that the trace with -10 dBm input power has been smoothed.

A measurement with a higher input power is also run for the CBCPW resonator at 60K over the wide frequency range. The measured *Q*-values are compared with the low-power measurements in Figure 8.19(a). Increasing the input power from -10 dBm to more than +15 dBm slightly reduces the *Q*-values (see the fractional difference of *Q* in Figure 8.19(b)) and shifts the harmonics to lower frequency. Particularly, below 2 GHz, the difference of *Q*-values at the two power levels increases as the frequency goes lower. There are two reasons why the reduction of *Q* becomes more significant at the low frequency end. Firstly, the higher input power improves the signal-to-noise ratio and overcomes the overestimation of *Q*-value of a noisy resonance curve. More importantly, the nonlinearity of superconductors plays a role when the input power is sufficient high. It skews the resonance, and lowers the *Q*-values due to the increased surface resistance. For a skewed resonant peak, the effectiveness of either 3dB or Lorentzian acquisition-method is compromised. According to [6], the actual Q_L is smaller than the 3dB-Q_L in this case. A method based on a multi-bandwidth measurement and an extrapolation procedure has been proposed to extract *Q* from non-Lorentzian resonances[6].

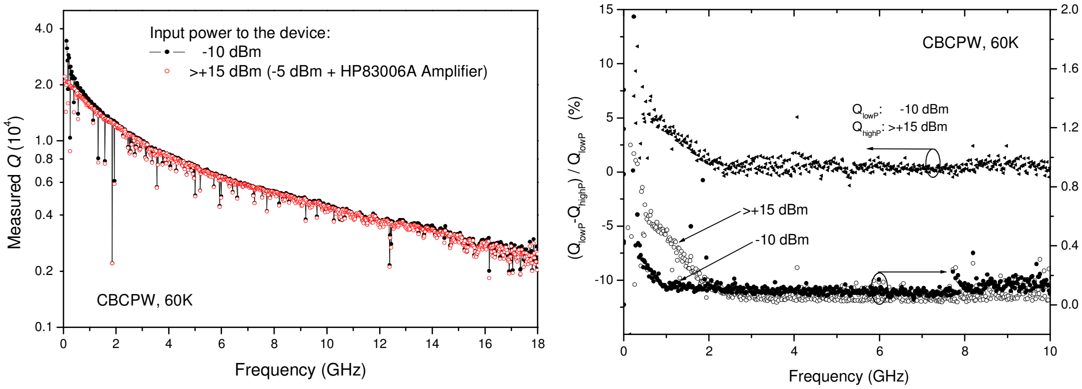

(a) (b)

Figure 8.19 (a) The measured *Q*-values of the CBCPW resonator at 60K with different input powers. (b) The percentage difference of the measured *Q*-values at the two different input powers, and the skew of the harmonics measured by $\Delta f_{cent}/BW_{3dB}$.

Unlike the split resonances described in Section 8.2.3.3, the skew of a resonance is not easily perceivable. So, a factor Δf_{cent} is defined here to quantify this.

Referring to Figure 8.2, let x_i be the decrement of S_{21} relative to the maximum value. The two interception frequencies f_1 and f_2 as a function of x_i can be determined as $f_1(x_i)$ and $f_2(x_i)$. Let $f_0(x_i) = [f_1(x_i) + f_2(x_i)]/2$. The standard deviation of a series of $f_0(x_i)$ (i=1…n, 0.8dB≤x_i≤3dB) is used to assess the skew. That is

$$\Delta f_{cent} = \left[\sum_{i=1}^{n} \left[f_0(x_i) - \bar{f}_0 \right]^2 \Big/ n \right]^{1/2}, \text{ where } \bar{f}_0 = \sum_{i=1}^{n} f_0(x_i) \Big/ n. \qquad \textbf{Equation 8-12}$$

If the resonance curve is symmetric, $\Delta f_{cent}=0$, otherwise $\Delta f_{cent}>0$. The magnitude of Δf_{cent} is a measure of the deviation from a symmetric resonance. In Figure 8.19(b), the skew of the harmonics at the two different input powers is plotted in terms of $\Delta f_{cent}/BW_{3\mathrm{dB}}$. From 2 to 18 GHz, $\Delta f_{cent}/BW_{3\mathrm{dB}}$ does not change much with frequency. The skew is insignificant and may just result from the uncertainty in measuring $f_0(x_i)$. However, there is a systematic increase of $\Delta f_{cent}/BW_{3\mathrm{dB}}$ at the low frequency end. At the higher input power, this increase emerges from 2 GHz, whereas at the low power it is only from 1 GHz. This is found to be correlated with the increased circulating power of the resonator at the lower frequencies.

It is the circulating power within the resonator rather than the input power to the test port that is more meaningful in comparing the power response of the resonators. The circulating power P_c is defined as the power travelling along the length of the resonator in the form of a standing wave. It can be expressed by[7]

$$P_c = \frac{W_0 v_g}{2l} = \frac{Q_L P_{in} |S_{21}| v_g}{\omega \cdot l} = \frac{Q_L P_{in} |S_{21}|}{\omega \cdot t_g} \qquad \textbf{Equation 8-13}$$

where W_0 is the stored energy of the resonator at the resonant frequency, given by

$$W_0 = \frac{Q_0 P_0}{\omega} = \frac{Q_0 P_{in} \left(1 - |S_{11}|^2 - |S_{21}|^2\right)}{\omega} = \frac{2 Q_L P_{in} |S_{21}|}{\omega} \qquad \textbf{Equation 8-14}$$

In deriving (8-14), the dissipated power P_0 of the resonator is expressed as the difference between the power P_{in} at the input port and the power reflected and transmitted. That is

$$P_0 = P_{in} \left(1 - |S_{11}|^2 - |S_{21}|^2\right)$$

The relation $|S_{11}| = 1 - |S_{21}|$ for a symmetrically coupled resonator is also applied. The circulating power in the CBCPW delay line resonator is plotted in Figure 8.20 as a function of the resonant frequency.

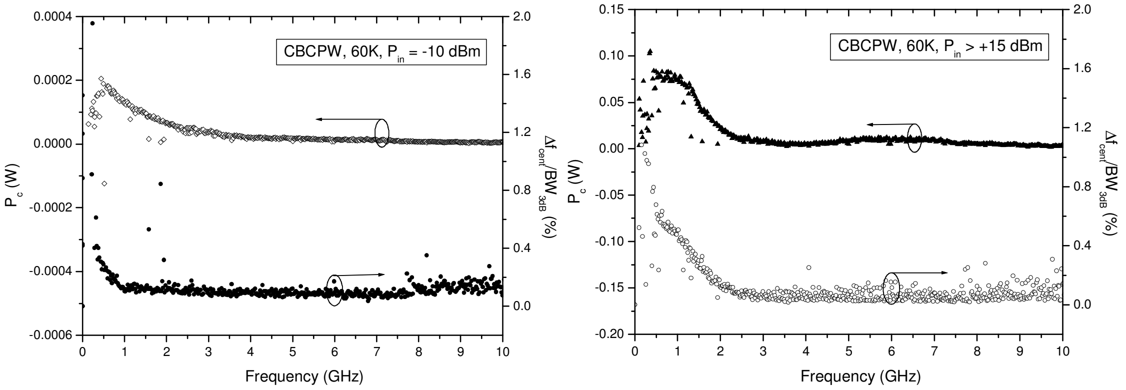

(a) (b)

Figure 8.20 The circulating power as a function of the resonant frequency: (a) at the low input power of -10 dBm; (b) at the higher input power, with the source power of -5 dBm boosted by the HP83006A Amplifier. The input power is at least +15 dBm, but not levelling at different resonant frequencies.

Good correspondence is found between the skew ($\Delta f_{cent}/BW_{3dB}$) and the circulating power (P_c), especially at the higher input power. With a low input power of -10 dBm, the circulating power in the delay line resonator is less than 3×10^{-4} W (-5.2 dBm) as shown in Figure 8.20(a). This power may be too low to incur nonlinear response. The increased $\Delta f_{cent}/BW_{3dB}$ in this case is more likely a result of the measurement uncertainty due to the noise in characterising the resonance. At the higher input power, however, the uncertainty due to noise can be neglected as the signal-to-noise ratio is significantly improved, therefore the increased skew (Figure 8.20(b)) should be caused by the nonlinear response of the superconducting materials. If a TEM transmission line is assumed, the total current flowing in the resonator can be expressed as[5]

$$I = \sqrt{\frac{4P_{in}Q_L S_{21}}{n\pi Z_0}} \qquad \textbf{Equation 8-15}$$

where n is the index of the harmonics. The average current density J_{av} in the central conductor can be estimated as the current I divided by the cross sectional area (line-width × film-thickness = 0.04 mm × 600 nm). In the case of Figure 8.20(b), the maximum J_{av} is ~4×10^5 A/cm^2 at 0.36 GHz. It is important to note that the actual current is not uniformly distributed and peaks at the edges of the conductor. The maximum current-density should be higher than J_{av} and dominates the microwave response and power dependence. As discussed in [3], the current-density distribution on a superconducting CPW can be calculated using the method of coupled transmission lines[8].

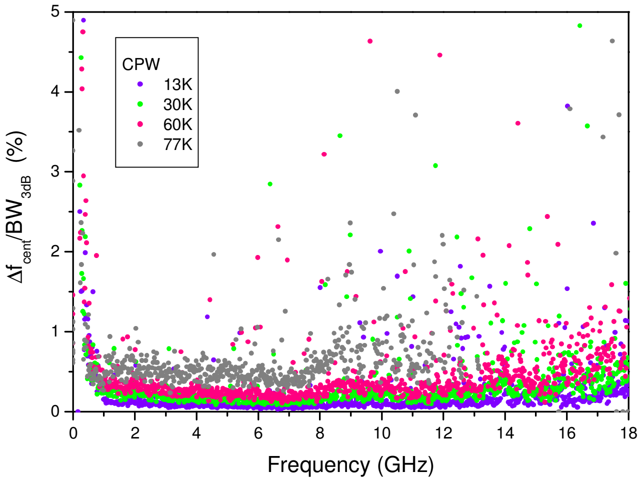

Figure 8.21 The skew of the harmonics measured at different temperatures for the CPW delay line resonator. The input power is -10 dBm.

As shown in Figure 8.21 for the CPW resonator, the skew ($\Delta f_{cent}/BW_{3dB}$) increases with temperature. It is less than 0.5% below 60K, and 1% at 77K. The increased skew at the low frequency end is due to the same reason as in the CBCPW. The scattered points are correlated with those of anomalous *Q*-values. It is also found that the harmonics of the CPW resonator give slightly larger values of $\Delta f_{cent}/BW_{3dB}$ than the CBCPW resonator. Generally, it is believed that the nonlinearity of superconductors is insignificant except at the low frequencies for both coplanar line resonators. The measurements are largely taken in the linear region.

8.5 Group delay

Once the harmonics of the delay line resonators are properly recorded and indexed, the wavelength λ_n is given by (8-1) and the phase velocity $\upsilon_{p,n}$ can be calculated by

$$\upsilon_{p,n} = \omega_n / k_n = \lambda_n \cdot f_n$$ **Equation 8-16**

where *n* is the index of each harmonic. The group delay can be evaluated from the discrete resonant frequencies by

$$t_{g,n} = \frac{1}{2}\left(\frac{1}{2 \cdot \Delta f_n} + \frac{1}{2 \cdot \Delta f_{n-1}} \right)$$ **Equation 8-17**

where $\Delta f_n = f_{n+1} - f_n$ and f_1 is the resonant frequency of the fundamental mode. The group velocity becomes

$$v_{g,n} = l / t_{g,n} \qquad \textbf{Equation 8-18}$$

where l is the total length of the delay line. Figure 8.22 shows that the group delays of both resonators, evaluated using (8-17), increase by less than 2 ns from 20 MHz to 18 GHz. From 30 K to 77 K, the group delay increases by 0.2 ns mainly over the range between 60K and 77K, due to the change of kinetic inductance of the HTS. From Figure 8.23, it can be seen that the CBCPW resonator has slightly smaller dispersion than the CPW, in terms of the variation of group delay with frequency.

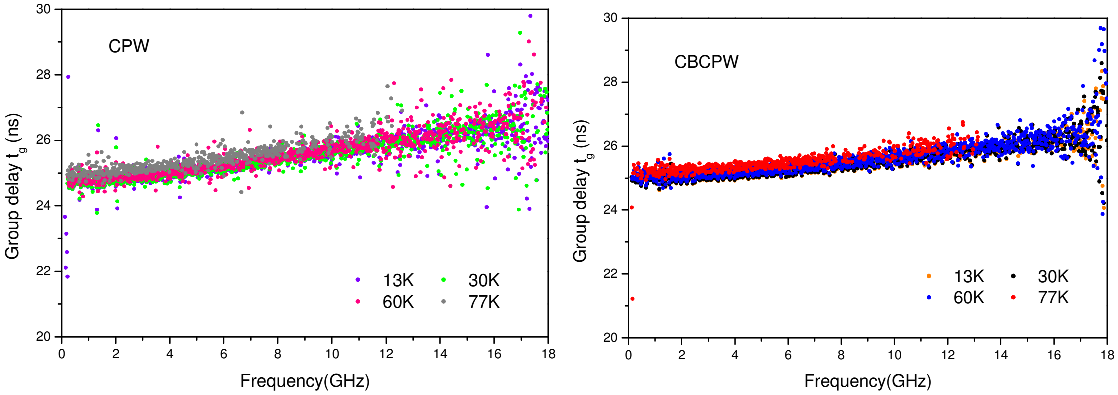

(a) (b)

Figure 8.22 Group delays of (a) the CPW delay line resonator and (b) the CBCPW delay line resonator.

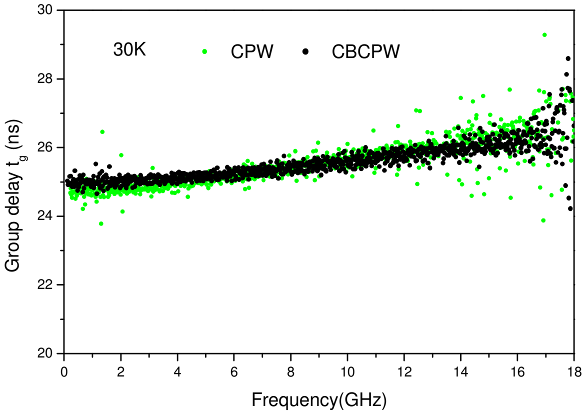

Figure 8.23 Comparison of the dispersion between the CPW and CBCPW resonator in terms of the variation of group delay with frequency.

The phase velocity from (8-16) and group velocity from (8-18) are compared in Figure 8.24(a) for the CBCPW resonator. The difference between the two values becomes more obvious as the frequency goes higher. This is an indication of more dispersion, which results from increasingly stronger cross-coupling with frequency. In Figure 8.24(b), the phase velocities of the CBCPW and CPW are compared. At the low frequencies, the wave in the CBCPW travels slightly slower than in the CPW due to the higher effective permittivity. This difference tends to disappear at high frequencies. This indicates that the conductor backing has more influence on the field distribution at the lower frequency. For a straight CBCPW transmission line of the same dimension as the experimental device (w=0.04 mm, s=0.074 mm), the phase velocity is ~0.285·c (c is the light velocity) according to conformal mapping calculation, which is smaller than the values shown in Figure 8.24. This is because the cross coupling present in the meander line of the experimental device speeds up the travelling wave.

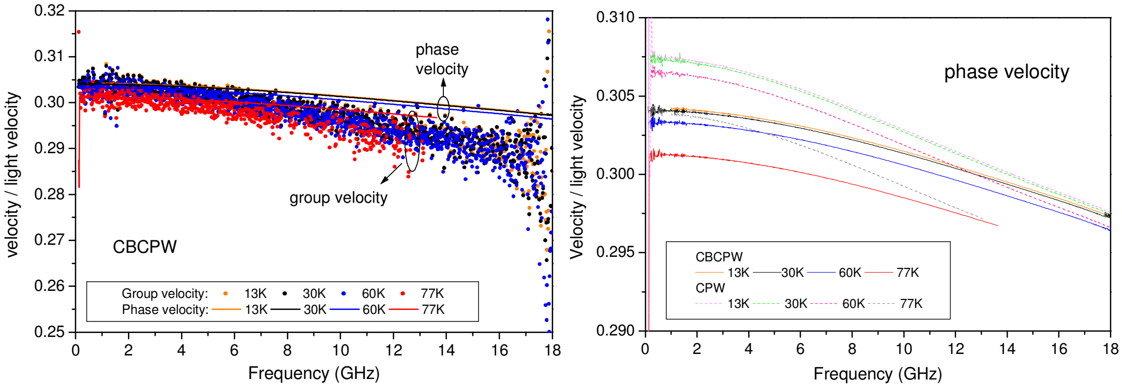

(a) (b)

Figure 8.24 (a) Comparison between the group velocity and phase velocity for the CBCPW delay line resonator. (b) Comparison of the phase velocity between the CPW and CBCPW delay line resonators.

8.6 Attenuation and surface resistance

8.6.1 Calculation of R_s from Q

To find the attenuation per unit length of a transmission line resonator from the Q-value, a TEM model[9] is used and the attenuation coefficient is expressed as

$$\alpha_{tot} = 8.68 \cdot \pi \cdot f / Q_0 / v_g$$ **Equation 8-19**

where α_{tot} is in dB/m, Q_0 is the unloaded quality factor and υ_g the group velocity of the transmission line resonator. This equation is slightly different from the form commonly used in the textbook, i.e. $\alpha = 8.68 \cdot \beta/(2Q_0) = 8.68 \cdot \pi \cdot f/Q_0/\upsilon_p$ [9], by involving the group velocity rather than phase velocity. This is required in order to take into account the dispersion. The detailed derivation of (8-19) is given in Appendix E. In terms of the attenuation per unit time delay,

$$\alpha_{tot}^{t} = \alpha_{tot} \cdot \upsilon_g = 8.68 \cdot \pi \cdot f/Q_0 \qquad \textbf{Equation 8-20}$$

It should be emphasized that α_{tot} is the total attenuation, including the contributions from the conductor loss, dielectric loss and radiation loss. The radiation loss is difficult to quantify analytically. Its contribution can be disregarded because it is very small as discussed in the context of Figure 8.11. The attenuation α_d due to the dielectric loss is given by (4-15) with ε_r=23.6, $\varepsilon_{eff} \approx (\varepsilon_r+1)/2$, and tan(δ)=$10^{-5}$ for a $LaAlO_3$ substrate. In this case, α_d is much smaller than α_c as shown in Figure 4.6. The attenuation due to the conductor loss therefore becomes

$$\alpha_c = \alpha_{tot} - \alpha_d = 8.68 \cdot \pi \cdot f/Q_0/\upsilon_g - \alpha_d \qquad \textbf{Equation 8-21}$$

According to (4-10), the surface resistance can be written as

$$R_s = \alpha_c / 8.68 / GF_c \qquad \textbf{Equation 8-22}$$

More generally, the left-hand side of (8-22) should be the effective surface resistance R_f of a thin film, which takes the effect of finite conductor thickness into account. However, the YBCO film used in this work, which has a thickness of 600nm (the penetration depth is ~200 nm), behaves effectively like a bulk superconductor as argued in Section 3.2.5. Therefore, R_f can be approximated to R_s. This will not change the frequency dependence anyway, because the relationship between R_s and R_f is frequency independent according to (3-36). The geometric factor GF_c based on (4-14) is used here to calculate R_s. This has been listed in the first column of Table 4-4. The geometric factor depends on the temperature.

The experimental errors in measuring Q-values can be propagated to the surface resistance. According to (8-21) and (8-22) and ignoring the uncertainty of resonant frequency f and group velocity v_g, one has

$$\left|\Delta R_s / R_s\right| = \left|\Delta\alpha_{tot} / \alpha_{tot}\right| = \left|\Delta\alpha_c / \alpha_c\right| = \left|\Delta Q_0 / Q_0\right| \qquad \textbf{Equation 8-23}$$

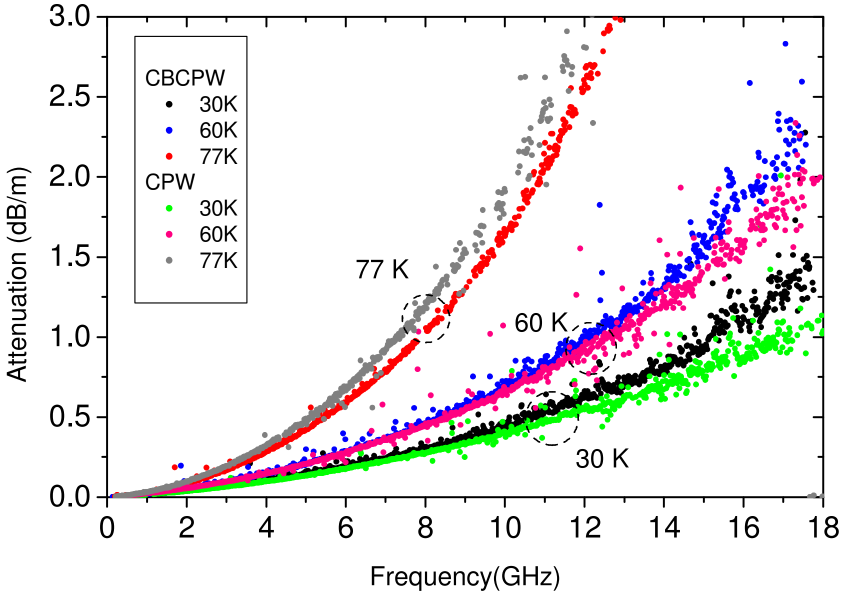

Figure 8.25 Attenuation coefficients for the CPW and CBCPW delay line resonators at different temperatures. The evaluation is based on (8-19) and the *Q*-values are acquired using Lorentzian method.

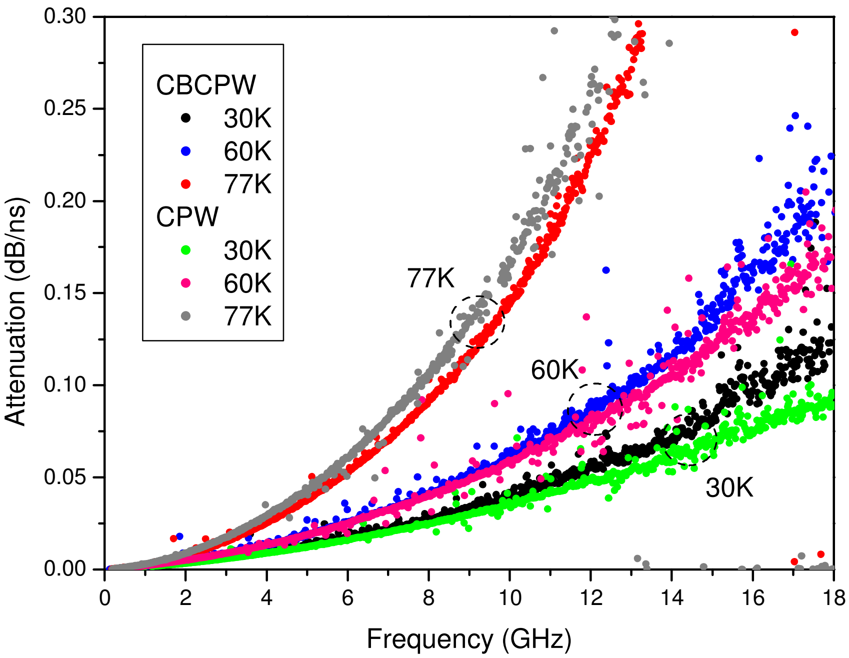

Figure 8.26 Attenuation per unit delay time, evaluated using (8-20).

8.6.2 Results

8.6.2.1 Attenuation

The attenuation per unit length of the delay line calculated from (8-19), and the attenuation per unit delay from (8-20) are shown in Figure 8.25 and Figure 8.26. These values at 10 GHz are listed in Table 8-2.

Table 8-2 Attenuation coefficients at 10 GHz for the CPW and CBCPW delay line resonators.

	CPW		CBCPW	
	α_c (dB/m)	α_c^t (dB/ns)	α_c (dB/m)	α_c^t (dB/ns)
30K	0.41	0.035	0.46	0.041
60K	0.66	0.059	0.68	0.061
77K	1.91	0.167	1.63	0.144

At 30K and 60K, the CPW has smaller attenuation than the CBCPW over most of the frequency range. According to the calculation in Section 4.2.2.3 and Appendix A, the conductor backing of the CBCPW only causes 2% loss increment, still not being able to account for the small difference in the attenuation between the CPW and CBCPW. The various qualities between individual films and substrates may have some contribution. In addition, it should be noted that the losses from the non-superconducting conductive films (used for grounding, as shown in Figure 7.6) might play a more important role on the different attenuations. Extra resistive loss would be incurred in the return current path by the presence of the conductive films. Because more films are used in the CBCPW device in order to interconnect the upper and lower ground planes, more such resistive loss should be expected in the corresponding resonator. At 77 K, the CPW shows unexpectedly higher attenuation than the CBCPW. The reason is not yet clear, but could be due to small variations in the transition temperatures of the two circuits or the temperature instability in the measurements. According to Figure 8.16(a) and equation (8-23), one Kelvin's temperature uncertainty at 77K may cause 11% fractional difference in both the Q-values and attenuation.

8.6.2.2 Surface resistance

Figure 8.27 shows the surface resistance of the superconductor as a function of frequency, estimated using (8-21) and (8-22). Since the present analytical models cannot fully account for the difference in the attenuation between the CPW and CBCPW, the surface resistances acquired from these two resonators are slightly different as shown in Figure 8.27. The obtained surface resistances at 10.9 GHz are given in Table 8-3, in comparison with the nominal values provided by the manufacturer of the thin films, which are measured using dielectric resonator method[10]. According to Figure 8.16(a) and equation (8-23), one Kelvin's temperature uncertainty will result in 11% fractional error in R_s at 77K and 2% at 30 K and 60 K.

Table 8-3 The obtained surface resistance (in μΩ) of 600 nm thick YBCO film on $LaAlO_3$ at 10.9 GHz.

T(K)	This work (CPW) [a]	This work (CPW) [b]	This work (CBCPW) [c]	Manufacturer [d]
30	166	198	220	180
60	268	347	361	250
77	873	1138	961	420

[a] GF_c based on equation (4-12) using the direct method for normal metals;
[b] GF_c based on equation (4-14) for the superconducting CPW;
[c] GF_c based on equation (4-14), multiplied by a factor 1.02 in order to account for the 2% loss increment caused by the conductor backing, as discussed in Section 4.2.2.3;
[d] Theva Dünnschichttechnik GmbH, Germany.

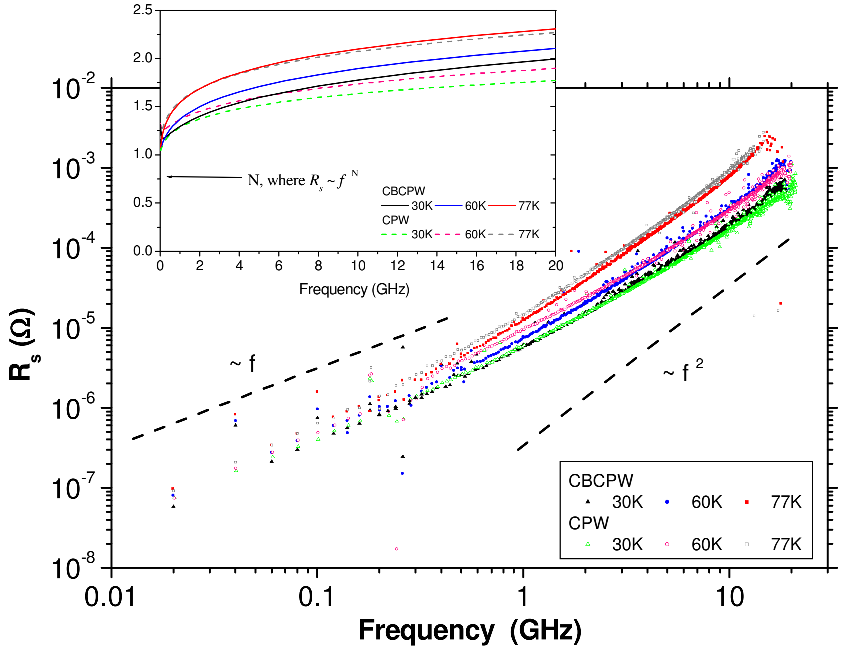

Figure 8.27 Surface resistance evaluated from the measured *Q*-values of the CPW and CBCPW delay line resonators. The geometric factors are based on the method for HTS CPW as discussed in Section 4.2.2.1 by Equation (4-14). The temperature-dependent values of the geometric factors are given in Table 4-3. The inset shows the frequency dependence of R_s in terms of the power *N*, if R_s is regarded to be proportional to f^N. These results are based on the measurements with an input power of -10dBm.

The obtained surface resistance very much depends on the geometric factor GF_c. As listed in Table 4-4, three methods can be used to calculate the geometric factor of a coplanar waveguide. The one based on (4-14) is formulated for superconductors, taking into account the field penetration. The other two, based on (4-11) and (4-12), are originally for normal conductors. For the coplanar structure used here, if R_s is extracted using (4-12), the result would be 20% smaller than that from using (4-14) and the result from using (4-11) would be 30% smaller. The R_s-values calculated by (4-12) are also included in Table 8-3.

Figure 8.27 shows the surface resistance against the frequency in a *log-log* scale. If the frequency-dependence of R_s takes the form f^N, by curve fitting, one can find the power N at different frequencies, as given in the inset of Figure 8.27. It can be seen that R_s is more of a f-dependence at the low frequency end, taking a power N of 1.1-1.2. N increases with frequency and tends to saturate. This is somewhat consistent with the implication that R_s is proportional to f at a high power level (nonlinear region), as mentioned in [1] and its references by Oates *et al.*[11] However, as discussed in the context of Figure 8.20(a), with an input power of –10dBm, the circulating power seems to be very low (less than 3×10^{-4} W) even at the low frequency end. Therefore, it is not yet understandable if nonlinearity really causes the quasi-linear dependence at the low end.

These results do not give a consistent f^2-dependence even at higher frequencies (low circulating power), as it should be, according to the two-fluid model. Both experimental errors in measuring Q-values and the deficiency of the transmission-line model used to formulate GF_c could affect the accuracy of R_s. These are discussed as follows.

At the low frequency end of the measurements, poor signal-to-noise ratio could have resulted in overestimated Q-values as discussed in the context of Figure 8.12. But this would not contribute to the surface resistance varying slower than f^2. RF leakage, which possibly causes those anomalous Q-values below 0.5 GHz (see Figure 8.7 and Figure 8.8) may lead to lower than expected Q-values. This can contribute to a slower varying R_s. Above all, if the input power is sufficiently high, which might not be the case in Figure 8.27, nonlinearity of the superconductor can skew the resonance, reduce the Q-value, and therefore, R_s will be overestimated.

In addition to these experimental problems, the transmission-line model used to extract R_s has its own limitations. Firstly, the acquisition accuracy, especially at high frequencies, may be affected by the presence of mutual coupling between adjacent segments of the meander delay-line resonators. On the one hand, this coupling increases signal dispersion, which can be properly considered in (8-19) by the frequency-dependent group velocity v_g. Between 2-18 GHz, v_g varies by less than 8%. On the other hand, the coupling rearranges the current distribution and therefore affects the geometric factor directly, which cannot be treated by available analytical models, as all are intended for straight transmission lines. To find the applicable range of the analytical geometric factor, the conductor loss of a 2.5ns coplanar meander line is calculated via full-wave simulations and compared with that predicted analytically, as shown in Figure 8.28. These two calculations agree well with each other up to 14 GHz. Above 14 GHz, the analytical loss becomes slightly higher than the simulated. This means the formula yields a larger geometric factor. Using this geometric factor to calculate R_s by (8-22) will be subject to underestimation. This deficiency of the analytical model has not been overcome yet. In order to find a geometric factor including the coupling effect, the current distribution in a pair of coupled lines carrying opposite electrical currents needs to be established.

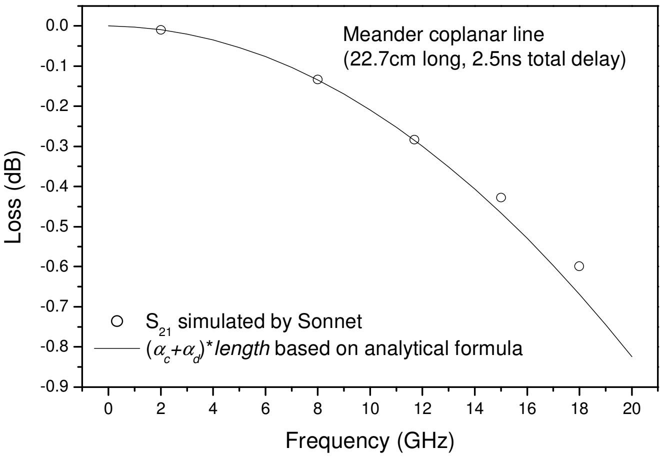

Figure 8.28 Comparison of analytically calculated loss with full-wave simulation. The simulated loss is obtained as the difference between a lossless S_{21} and a S_{21} with R_s=110 µΩ at 7.95 GHz and tanδ=10^{-5}. The f^2-dependence of R_s is applied. The ripple of the simulation results (0.04 dB) is negligible. The CPW meander line width is 0.02 mm and slot width 0.04 mm.

Secondly, the large number of bends in the meandered structures complicate the characterisation. Both the reflection due to discontinuity and the extra loss due to current crowding at the corners of the bends may contribute to the attenuation, which were not taken into account. In principle, equation (8-21) is only applicable if these losses from the bends are deducted from the total attenuation. It is believed that current crowding is more of a problem, and it would have more effect as the frequency goes higher.

Finally, the increasing superposition between adjacent resonances slightly overestimates the Q-values as discussed in the context of Figure 8.13. The surface resistances calculated from (8-21) and (8-22) are therefore subject to small underestimation for this.

Table 8-4 summarises the factors affecting the acquisition accuracy of surface resistances. At the low frequency end, the dominant factors are more likely to be the nonlinearity of HTS and the RF leakage, whereas at high frequencies, the deficiency in treating the mutual coupling and bends may be the main factor. It should be noted that the divergent frequency-dependences at different temperatures are not yet understood. Further experimental investigations are needed.

Table 8-4 Estimation errors of the surface resistance caused by different factors at different frequency ranges and power levels. (For this measurement, the low input power is at –10dBm and the high power is at least +15dBm.)

<Surface resistances>	**Low frequency**		**High frequency**	
	Low power	**High power**	**Low power**	**High power**
Poor signal-to-noise ratio	*Underestimation*	--	--	--
Nonlinearity of HTS	*Overestimation (uncertain)*	*Overestimation*	--	--
Superposition of adjacent harmonics	--	--	*Underestimation (small)*	*Underestimation (small)*
Deficiency of the analytical model in considering the coupling effect	*Underestimation (small)*	*Underestimation (small)*	*Underestimation (bigger)*	*Underestimation (bigger)*
RF leakage	*Overestimation*	*Overestimation*	--	--
Reflections and current crowding at bends of meanders	*Overestimation (small)*	*Overestimation (small)*	*Overestimation (bigger)*	*Overestimation (bigger)*

8.7 Summary

Two 25 ns (2.28m) HTS coplanar delay line resonators, one with conductor-backing (CBCPW) and the other without (CPW), are characterized from 20 MHz to 20 GHz at 30, 60 and 77 K using the resonator technique. The quality factors and the resonant frequencies are measured. The attenuation is estimated and the surface resistance of the superconductor is extracted based on TEM transmission line model. The main findings of this chapter are:

1) The resonant frequency of the fundamental mode at 30K is 20.2540 MHz for the CPW resonator and 20.0458 MHz for the CBCPW resonator.

2) There are anomalous points observed in the measured graphs of Q-values as a function of frequency. The mechanisms of these anomalies are different between the CPW and CBCPW resonators. The CBCPW resonator is less affected by parasitic modes, while the CPW resonator may be significantly affected by the slotline modes, resulting in split resonance peaks.
3) The measurement results do not give a profile of f^2-dependence. At the low frequency end, it is more like a linear dependence. Both experimental errors in measuring Q-values and the deficiency of the transmission-line model used to formulate GF_c could have affected the accuracy of R_s. The major sources of errors may be the nonlinearity of HTS and the RF leakage at the low frequency end, and the deficiency in treating coupling and bends at high frequencies.
4) The fractional shift of resonant frequency with temperature is independent of frequency, which indicates a frequency-independent penetration depth of the superconductor.
5) The skew of the harmonics increases with temperature and circulating power. But the overall skew is insignificant excepted at the low frequency end, where the circulating power increases rapidly. This is an indication of the nonlinear response of superconducting materials. Nevertheless, it is believed that the measurements from 2 to 18 GHz are still in the linear region of the superconductor. Below 2 GHz, the nonlinearity becomes prominent for the measurements with an input power of more than +15dBm.
6) The dispersion of both resonators is less than 8% in terms of the variation of group delay with frequency. The group delay increases by less than 2 ns from 2 to 18 GHz.
7) The CBCPW resonator shows slightly higher attenuation than the CPW resonator. At 10 GHz, the attenuation of the CPW resonator is 0.41dB/m (0.46dB/m for CBCPW) at 30 K and 0.66dB/m (0.68dB/m for CBCPW) at 60 K.

Limitations of this characterisation using resonator techniques are:

1) The external coupling is very weak, so the signal-to-noise ratio of the measurement is poor below 1 GHz or at 77K, which causes some experimental uncertainty.
2) The origins of the parasitic modes causing the anomalous Q-values are not fully

understood.

3) The difference in attenuation between the CPW and CBCPW structures cannot be solely accounted for by the loss from the conductor backing.

4) The geometric factor used to extract R_s from the measured Q-values does not take fully into account the cross coupling, and the losses due to reflection and current crowding at bends of the meander line structure.

---

[1] Z.-Y. Shen, *High-temperature superconducting microwave circuits*, Artech, 1994.

[2] P. J. Petersan, S. M. Anlage, “Measurement of resonant frequency and quality factor of microwave resonators: comparison of methods”, *J. Appl. Phys.*, vol. 84, no. 6, pp. 3392-3402, Sept. 1998.

[3] D. W. Huish, “Microwave and optical reflectance studies of YBCO films”, PhD thesis, the University of Birmingham, UK, 2003.

[4] D. Kajfez, S. Chebolu, M. R. Abdul-Gaffoor, A. A. Kishk, “Uncertainty analysis of the transmission-type measurement of *Q*-factor”, *IEEE Trans. Microwave Theory Tech.*, vol. 47, no. 3, pp. 367-371, Mar. 1999.

[5] M. J. Lancaster, *Passive microwave device applications of high-temperature superconductors*, Cambridge University Press, Cambridge, UK, 1997, pp. 136-142.

[6] X. S. Rao, C. K. Ong, Y. P. Feng, “*Q*-factor measurement of nonlinear superconducting resonators”, *Electronics Letters*, vol. 36, no. 3, pp. 271-273, Feb. 2000.

[7] Z.-Y. Shen, C. Wilker, P. Pang, W. L. Holstein, D. W. Face, D. J. Kountz, “High T_c superconductor-sapphire resonator with extremely high *Q*-values up to 90K”, *IEEE Trans. Microwave Theory Tech.*, vol. 40, pp. 2424-2432, 1992.

[8] A. Porch, M. J. Lancaster, R. G. Humphreys, "The coplanar resonator technique for determining the surface impedance of $YBa_2Cu_3O_{7-\delta}$ thin film", *IEEE Trans. Microw. Theo. Tech.*, vol. 43, no. 2, pp. 306-314, 1995.

[9] D. M. Pozar, *Microwave engineering*, Addison-Wesley, 1990, pp. 338

[10] J. Krupka, M. Klinger, M. Kuhn, A. Baranyak, M. Stiller, J. Hinken, J. Modelski, “Surface resistance measurements of HTS films by means of sapphire dielectric resonators”, *IEEE Trans. on Appl. Supercond.*, vol. 3, no. 3, pp.3043-3048, Sept. 1993.

[11] D. E. Oates, A. C. Anderson, P. M. Mankiewich, “Measurement of the surface resistance of $YBa_2Cu_3O_{7-x}$ thin films”, *J. Supercond.*, Vol. 3, 251-259, 1990; D. E. Oates, P. P. Nguyen, G. Dresselhaus, M. S. Dresselhaus, C. W. Lam, S. M. Ali, “Measurements and modelling of linear and nonlinear effects in striplines”, *J. Supercond.*, vol. 5, pp. 361-369, 1992; D. E. Oates, P. P. Nguyen, G. Dresselhaus, M. S. Dresselhaus, C. C. Chin, “Nonlinear surface resistance in $YBa_2Cu_3O_{7-x}$ thin films”, *IEEE Trans. Appl. Supercond.*, vol. 3, no. 1, pp. 1114-1118, Mar. 1993.

Chapter 9 Measurements of HTS Delay lines

9.1 Introduction

This chapter presents the measurement results in both the frequency and time domains for two HTS delay lines. These include the key parameters for a delay line, such as the bandwidth, transmission loss, ripple, group delay, and dispersion. The bandgap and bandstop of the coplanar delay lines were characterised. The box modes, radiation, and power dependence of the delay lines were also investigated.

In the application, a delay line operates in a full transmission state as opposed to the resonant state discussed in the previous chapter. This has been achieved by connecting the sliding contacts of the K-connectors with the superconducting coplanar line using silver-loaded epoxy, after the resonance measurements were completed. The experimental fixture was set up as in Figure 7.9, and low temperature calibrations as described in the context of Figure 7.10 were performed.

For a wideband measurement, choosing appropriate sweep frequency step is very important as it determines the resolution of the measured S parameters. For most of the work reported in this chapter, calibrations were performed in three consecutive frequency ranges: 0.05-8.05 GHz, 8.055-16.055 GHz, and 16.06-24.06 GHz, with 1601 data points in each section. So, the frequency step is 5.0 MHz. In the frequency-domain response, a feature with a bandwidth narrower than this will be difficult to resolve. The experimental results are based on this multisection calibration unless otherwise stated.

9.2 Frequency domain measurements

The S_{21} responses of both coplanar delay lines, measured at 30, 60, and 77K, are shown in Figure 9.1. The measured reflection responses (S_{11} and S_{22}) are shown in Figure 9.2. No bonding wires were used to balance the in-plane grounds of either of the delay lines. Low-temperature calibrations were performed. It is worth mentioning that the effectiveness of the reflection calibrations for S_{11} and S_{22} may not be as good as the transmission calibrations for S_{21}. This could be the cause of the unphysical positive dB-values of the reflection coefficients at ~19 GHz in Figure 9.2. The SMA-short used for reflection calibration has a specified operation frequency up to 18 GHz, which may not be good enough for higher frequency measurements.

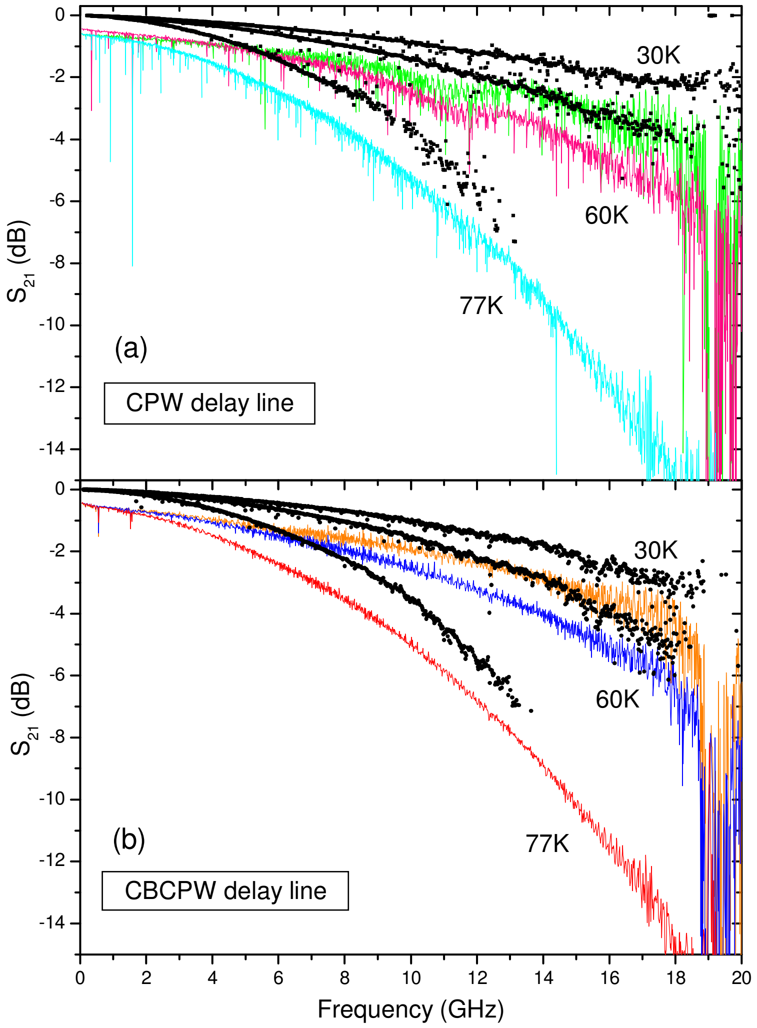

Figure 9.1 Measured S_{21} responses (colour lines) of the CPW and CBCPW HTS delay lines at 30, 60, and 77K, compared with the transmission losses (black lines) estimated from the measurements of both delay lines as resonators (Chapter 8). The frequency step of the shown S_{21} is 5.0 MHz.

To enhance the resolvability of the possible transmission notches with very narrow bandwidth, measurements have also been taken at a finer frequency step of 0.625 MHz (1601 points per 1 GHz) up to the frequency of 24 GHz, as shown in Figure 9.3. For the CBCPW delay line, there is no loss of detail over the frequency range of 2 to 20 GHz by the 5.0 MHz steps used in Figure 9.1(b), as compared with Figure 9.3(a). Only below 2 GHz can more transmission notches be found with a finer frequency sweep. However, for the CPW delay line, as shown in Figure 9.3(b), a finer frequency sweep shows more transmission notches than in Figure 9.1(a) over the same band of interest.

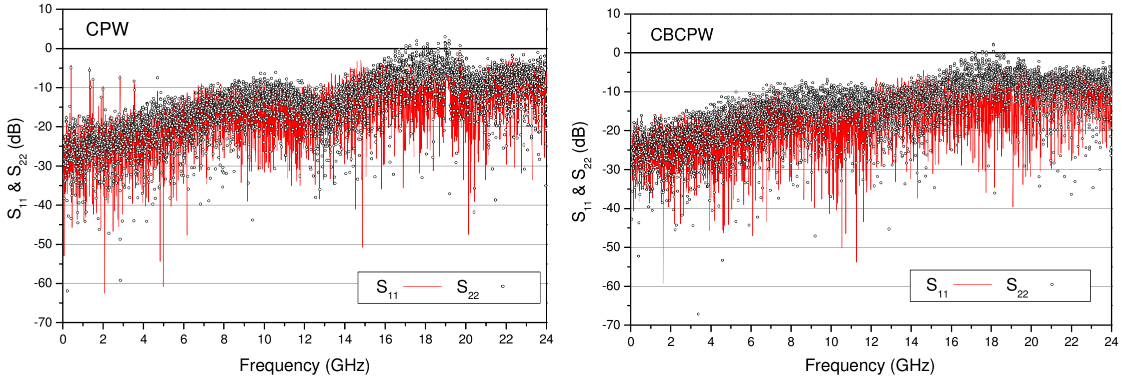

(a) (b)

Figure 9.2 Measured reflection responses at 30K. The frequency step is 5.0 MHz.

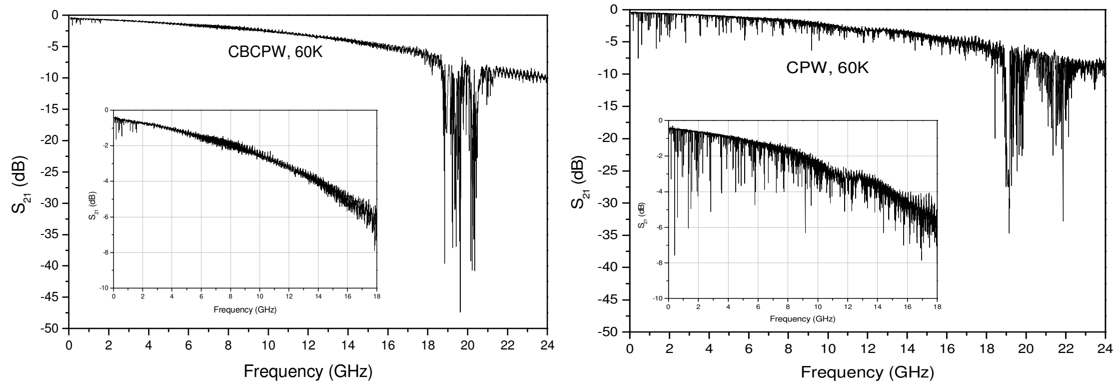

(a) (b)

Figure 9.3 Measured S_{21} of the CBCPW and CPW delay lines using a finer sweep with a frequency step of 0.625 MHz.

9.2.1 Resonance-free bandwidth

Without using wire-bonding to balance the in-planar grounds, the CBCPW delay line achieves a resonance-free passband from 2 to 18 GHz as shown in Figure 9.1(b). This is the widest ever demonstrated on superconducting delay lines. The bandwidths of previous superconducting delay lines (Table 2-1) were no more than 7 GHz. The passband of the CBCPW delay line is only limited by a bandgap at around 19 GHz. This agrees very well with the simulations in Figure 5.7. The high reflection around 18 GHz (see Figure 9.2) may be partly due to the increased coupling as the short meander segments are close to a quarter-wavelength, and partly due to the mismatches at the input/output and the bends. The transmission notches below 2 GHz may come from a second transmission path from the input to output connectors through the metal box. To our best knowledge, this is the first coplanar delay line successfully demonstrated without using bonding wires. In fact, this is also the first delay line successfully achieved on a CBCPW structure.

In contrast to the conductor-backed coplanar delay line, the S_{21} responses of the CPW delay line in Figure 9.1(a) are dominated by many transmission notches. These notches can find their correlations at the same frequencies with the split resonant peaks observed in previous resonator measurements, which probably result from the power transfer into parasitic slotline modes. This has long been a challenge to the design of coplanar circuits. As discussed in Section 4.2.4, there have been several approaches to suppress these modes. However, for a complex coplanar structure, the only practical and also the most conventional way is to use bond-wires, equalizing the unbalanced potentials on the in-plane grounds at either side of the signal line. This was adopted in the references [1, 2, 3]. The disadvantage of using wire-bonds is the increased conductor loss and the occurrence of spurious resonances between the bonding wires. The bonding technique itself is also costly and risky. Encouragingly, comparative studies of the two types of coplanar delay lines reported here show that the CBCPW delay line is able to achieve a very wide band free from resonances. Considering the two delay lines share the same pattern and dimensions, it is reasonable to attribute the mode-suppression effect to the presence of the conductor backing in the CBCPW structure.

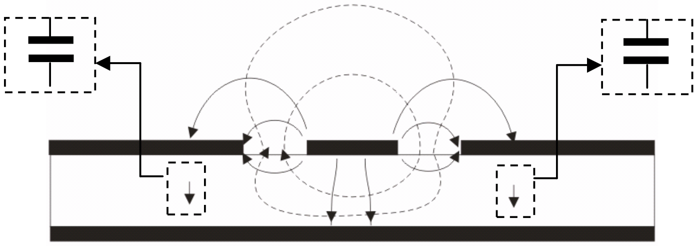

Figure 9.4 Illustration of the proposed “wireless” bonding effect of the conductor backing in a CBCPW.

Although it is always a great interest to understand this desirable effect, there has not been theory or definite experimental evidence to account for it. As mentioned in Section 4.2.4, Omar[4] reported that the top and bottom shields of a coplanar waveguide could reduce slotline modes. The bottom shield was actually a conductor backing. However, the mode-suppression effect could be achieved only if the shield was placed as close as possible to the coplanar slots[4]. It was suggested that the separation between the circuit and shields should be less than

w+2s^4. This is obviously not the case for the coplanar line reported here. Omar[4] explained the effect as an attenuation of slotline mode by the metal shields. But there is also a possibility that the coplanar structure effectively propagates a microstrip mode if the shield is too close to the coplanar structure.

According to the simulation results given in Figure 5.12, the CBCPW meander line has fewer transmission notches than the corresponding CPW structure using the same frequency steps. This cannot yet be taken as conclusive evidence of the conducting backing being able to suppress parasitic modes, because it remains difficult to determine whether these notches are related to slotline modes. However, there is a positive effect of the conductor backing, which has been indicated by both full-wave and conformal mapping calculations: the slightly weaker cross-coupling between a pair of CBCPW lines than for CPW, as shown in Figure 4.8. This suggests that the conductor backing does have a screening effect, a consequence of the overlapping field being reduced by the conductor backing, as illustrated in Figure 9.4. The capacitance between the upper and lower ground planes could be interpreted as a "wireless" interconnection of the in-plane grounds. This may qualitatively account for the suppression of slotline modes. However, it is worth mentioning that the CBCPW structure used in this work has a slot width much smaller than the substrate thickness, (Figure 9.4 is not to the scale.) so most of the electrical field still concentrates in the slots rather than down to the substrate. The capacitances between the ground planes are therefore expected to be small. Otherwise, the microstrip mode could be induced.

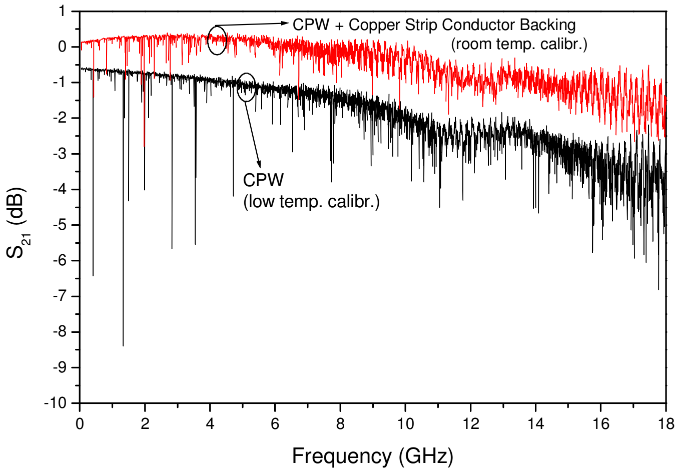

Figure 9.5 The CPW delay line attached with a piece of copper strip as a "conductor backing". The response of the modified CPW delay line is measured at 30K based on room temperature calibration. The frequency step of the shown S_{21} is 5 MHz.

Experimental attempts were made to look into the effect of conductor backing and bond wires on the performance of the CPW delay line. A "conductor backing" was made for the CPW delay line by sticking a piece of copper strip to the underside of the substrate. The measured response is shown in Figure 9.5 based on a room-temperature calibration. (The only effect of the room-temperature calibration is on the values of insertion losses without altering features such as ripples or transmission notches.) Fewer transmission notches were observed after the modification, which suggests a positive effect of reducing the spurious modes by the "conductor backing". However, more significant improvement in the response may be expected if the air gaps between the cooper strip and substrate can be eliminated, so that they would not compromise the function of the backing.

Eighteen crossover wires have also been bonded onto the CPW delay line at the bends close to the input/output and along the innermost semi-circles, using the gold pads shown in Figure 7.1(a) and Figure 7.5. However, it turns out to be inadequate to reduce the spurious modes. More crossover wires are needed periodically along the transmission line as Fenzi[3] did on the meandered CPW delay lines (Figure 2.6).

9.2.2 Transmission loss

At 10 GHz, the measured transmission loss of the CBCPW delay line is less than 0.08 dB/ns at 30K, 0.1 dB/ns at 60K, and 0.2 dB/ns at 77K. These are higher than the values (black lines in Figure 9.1(b)) estimated from the resonance measurements (Figure 8.25). The difference was proven to be due to a non-optimal resistive loss of the epoxy (used to connect the sliding contact with the coplanar line), rather than the superconductor circuit itself. The excess loss at the low frequency end (~0.5 dB in Figure 9.1(a) and (b)) was found in close correlation with the resistance of the epoxy. Measured at DC with a digital multimeter, it was 1.6 Ω for the CPW delay line and 2.3 Ω for the CBCPW line. Under optimal cure condition of the epoxy, this DC resistance should be less than 0.1 Ω and its loss is negligible. Therefore, it is expected that the transmission loss of the delay lines can be improved by 0.5 dB at low frequency and even more (1-2 dB) at higher frequencies, reasonably approaching the loss predicted by the resonance measurements, which is 0.041 dB/ns at 30 K, 0.061 dB/ns at 60 K, and 0.144 dB/ns at 77K. The only lower loss reported in other delay lines (Table 2-1) was the stripline YBCO delay line presented by Talisa[5]. That was ~0.06 dB/ns at 77K ignoring the resonances and ripples. However, the bandwidth of the stripline delay line was severely restricted by many transmission notches. A comprehensive comparison about the losses of different HTS delay lines has been given in Figure 2.7 and Table 2-1.

9.2.3 Ripples

For the CBCPW delay line, the ripples of the S_{21} responses are less than 1 dB up until 16 GHz. Near the bandgap, the ripples increase rapidly. This is partly caused by the increased reflections, and partly by the higher cross-coupling level as the quarter-wavelength approaches the coupled length l_c of the meander structure. The smallest ripple period is 20 MHz, as shown in Figure 9.6(a), and is due to the mismatches at the input/output. Slightly higher ripples with a period of 180 MHz can also be recognized, as in Figure 9.6(b). These result from a reflection along the meander line, which will be interpreted later in the time domain.

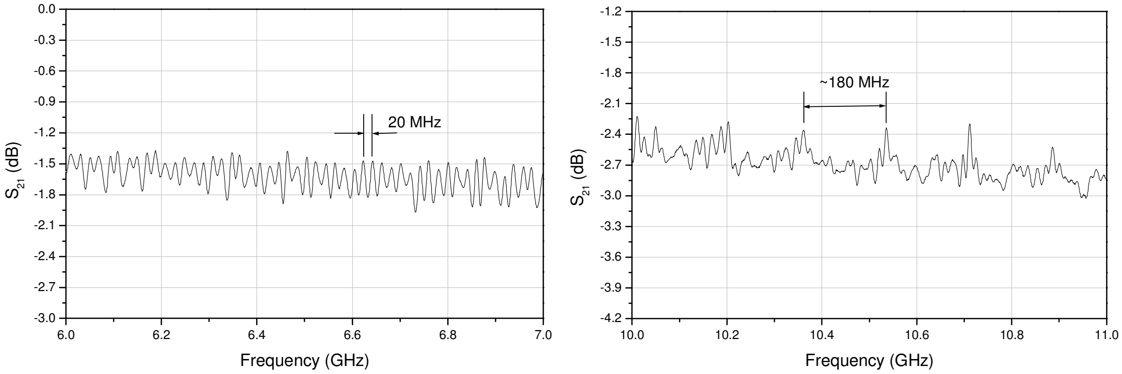

(a) (b)

Figure 9.6 Magnitude ripples in the measured S_{21} of the CBCPW delay line at 60K. The frequency step is 0.625 MHz.

9.2.4 Dispersion

In the frequency domain, the dispersion of the delay line can be assessed in terms of the variation of group delay with frequency. The group delay is calculated from the phase decrement with respect to frequency by (5-4). As shown in Figure 9.7(a), the group delays of both delay lines increase by less than 2 ns between 2 and 18 GHz. The group-delay spectra can be fitted into 2^{nd}-order polynomials as given in Figure 9.7(c). The ripples and anomalous points of scatter are closely correlated to those of the transmission responses. The ripples are mainly due to mismatch. The group delays from the transmission measurement are in good agreement with those extracted from the resonance measurement by (8-17). In Figure 9.7(b), the measured group delays are also compared with the calculation results from the simulated phase responses of the meander lines in Figure 5.7. Scaled by the ratio between the measured group delay and simulated one at 2 GHz, the simulated delay graph, as a function of frequency, agrees very well with the measurements over the entire band. Since the simulated meander line is not wound, it can be implied from this agreement that the dispersion of the double-spiral meander structure is mainly attributed to the coupling between the short meander segments. The coupling between the meandered spiral-turns has little effect. As the temperature changes from 30K to 77 K, the group delay increases slightly by 0.2 ns mainly over the range from 60K to 77K due to the change of kinetic inductance of the HTS.

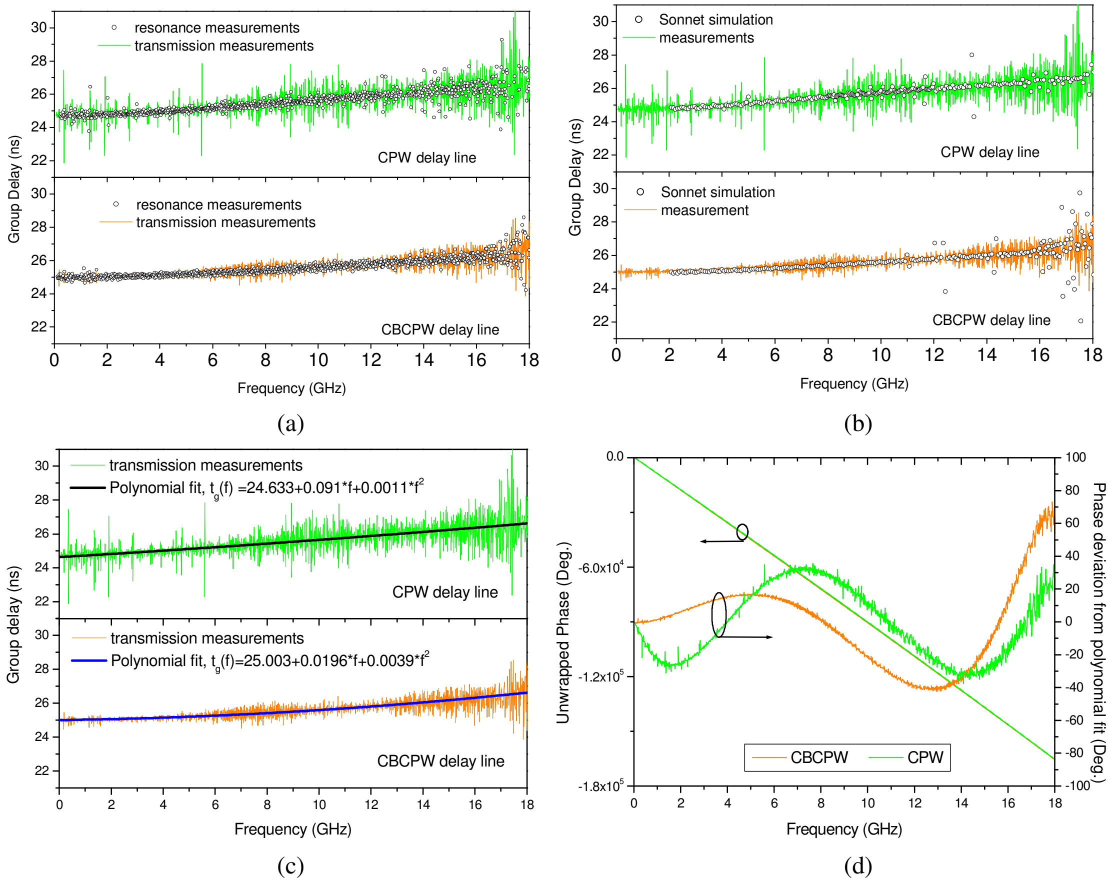

(a) (b)

(c) (d)

Figure 9.7 (a) Comparison of the measured group delay (30 K) with the values estimated from the resonant frequency measurements as shown in Figure 8.22; (b) Comparison of the measured group delay (30 K) with the values estimated from the full-wave simulations shown in Figure 5.10. For the CPW line, the simulation results were scaled from 1.23 ns at 2 GHz to 24.85 ns; for the CBCPW line, the simulation results were scaled from 1.25 ns at 2 GHz to 25 ns; (c) 2nd-order polynomial fit of the group delay spectra; (d) Unwrapped phase spectra and phase deviation from a polynomial fit.

The CBCPW delay line shows slightly smaller dispersion than the CPW as has also been observed in both the resonance measurements (Figure 8.23) and full-wave simulations

(Figure 5.10). The difference in the group delays is reduced as the frequency increases, and eventually the group delays of the CPW and CBCPW delay lines converge with each other. This is an indication that the conductor backing has more influence on the field distribution at lower frequencies.

The phase distortion is often a concern in communication systems. This can be characterized either by aforementioned group delay, or by phase ripples which can be seen in Figure 9.7(d). Figure 9.7(d) plots the deviation of the phase spectrum from a 3rd-order polynomial fit. The phase spectrum is unwrapped by numerically integrating the measured group delays. The small localised ripples are less than 5^{o} up to 15 GHz, 10^{o} up to 17 GHz, and 15^{o} up to 18 GHz for the CBCPW delay line. For the CPW, the ripples are bigger, but less than 20^{o}. As the details of these phase ripples are less likely to be reproducible from one delay line to another, this may have implications of the phase tracking. The physical meaning of the big fluctuation is not yet clear, neither its reproducibility.

9.2.5 Bandgap and bandstop

At around 19 GHz, bandgaps can be identified for both the CPW and CBCPW delay lines in Figure 9.1 and Figure 9.3. The detailed features are shown in Figure 9.8(a). There are clusters of transmission-notches around the bandgap. These mainly occur around 19.2 GHz and 21.5 GHz for the CPW delay line, but between 19 and 20.5 GHz for the CBCPW delay line. Beyond the bandgaps and below 24 GHz, the responses recover to the transmission state with a ripple of 2 dB.

Beyond 24 GHz, the CBCPW delay line shows a cut-off starting from 26 GHz, whereas the cut-off is from 30 GHz for the CPW delay line, as shown in Figure 9.8(b). The simulations in Figure 5.7 show that the stopband of both types of coplanar meander lines starts from 30 GHz. The unexpectedly lower cut-off frequency of the conductor-backed delay line may be related to the parallel plate mode, which may be established between the upper and lower ground planes. It should be pointed out that the features of the responses between 24 and 28 GHz were sensitive to the movement of the flexible cables (SUCOFLEX 104), interconnecting the network analyzer with the hermetic adaptors on the cryostat. This may be related to the excitation of higher-order modes in the coaxial cable, which has a maximum operation frequency specified at 26.5 GHz. Although the cables may also play a role beyond

28 GHz, the features of the responses did not exhibit sensitivity to the movable cable assemblies. There is no reason to believe the difference in the cut-off frequencies of the two delay lines were due to the cables, because the same assemblies and measurement arrangement were used. Box resonances and radiations do not contribute to the cut-offs either. No significant changes were observed after removing the box lids of the delay lines.

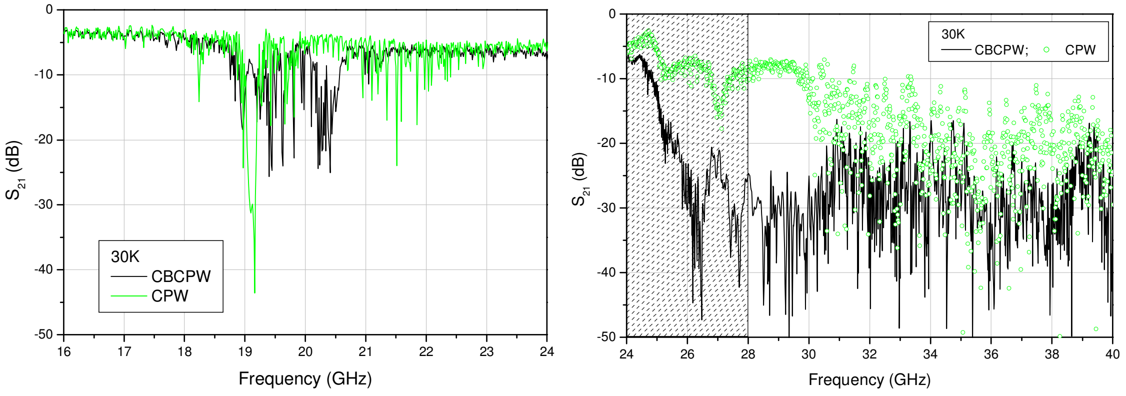

(a) (b)

Figure 9.8 (a) Measured bandgaps at around 19 GHz; (b) Measured bandstops. The features of the responses in the shadow area were sensitive to the movement of the flexible cables used in the measurements.

9.3 Time domain analyses

9.3.1 Time responses of delay lines

The time-domain responses are produced mathematically by the network analyser using the Fourier-transform technique on the measured frequency responses. The time-response resolution is defined as a measure of how close two transmitted or reflected signals can be and still be distinguished from each other[6]. For signals of equal amplitude, the resolution equals to the 50% (–6 dB) impulse width. It is inversely proportional to the frequency span of the measurement. The approximate formulas for calculating the time resolution are[6]

$$\frac{0.98}{\text{frequency span}}, \quad \text{for the "low - pass" mode;}$$

$$\frac{0.98}{\text{frequency span}} \times 2, \quad \text{for the "band - pass" mode.}$$

based on a normal windowing function[6] of the 8722ES network analyser. The measurement range in the time domain is the reciprocal of the frequency step. These parameters used in measuring the delay lines are listed in Table 9-1. The “low-pass” mode has a better resolution but its measurement time-range cannot cover the main transmitted signal (delayed by ~25 ns). It is only used to examine the reflections from the feed-line areas, which occur within a 2 ns time period.

Table 9-1 Resolution and range of the time domain responses for the delay lines measured using 8722ES network analyser.

Measurement mode	Frequency range	Number of data points	Frequency step	Time resolution	Time range
"Band-pass"	0.05-8.05 GHz, 8.055-16.055 GHz, 16.06-24.06 GHz	1601	5 MHz	0.245ns	200 ns
	2-18 GHz	1601	10 MHz	0.122 ns	100 ns
"Low-pass"	0.05-20.05 GHz	401	50 MHz	0.049 ns	20 ns

The measured transmission responses are shown in Figure 9.9(a), indicating a signal delay of 25.5 ns (signal T0) for both delay lines. Considering the total physical length of 2.28m, this gives an average signal velocity of 89.4 mm/ns. The noise level of the CPW delay line response is 15 dB higher than the CBCPW due to the anomalous transmission notches in the frequency domain. The small signal T2 and those behind are delayed due to multiple reflections, which can be interpreted better from the reflection responses. The proceeding signal T1 at ~2.4 ns is leakage due to backward coupling directly into the output port through the outermost semi-circles. The path of the signal is roughly illustrated in Figure 9.10. This signal (T1) is very weak and can stand out more clearly when the impulse bandwidth is reduced to 0-8 GHz. This spurious signal has been enhanced because there are two possible paths, one clockwise and the other anticlockwise. A non-symmetrical device would have been a better choice, as the signals would not have occurred at the same time.

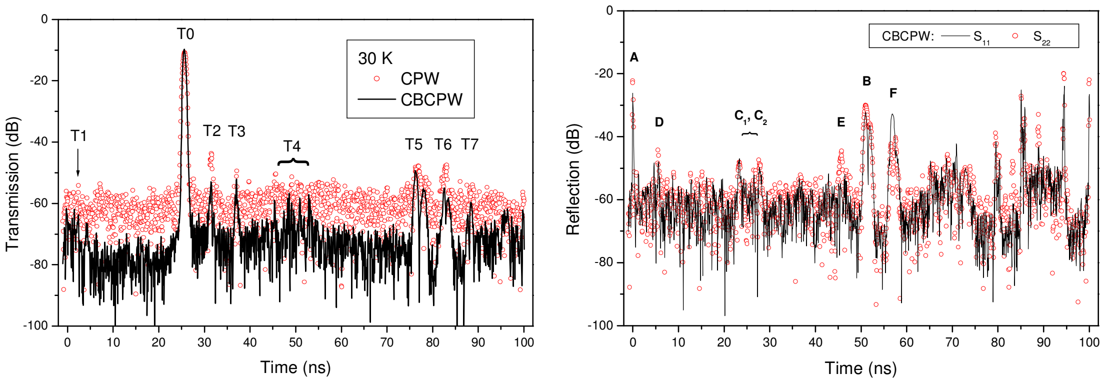

(a) (b)

Figure 9.9 Time domain responses at 30K (inverse Fourier transformed from the measured frequency domain responses between 2 and 18 GHz): (a) transmission responses of the CPW and CBCPW delay lines; (b) reflection responses of the CBCPW delay line seen from both ports. Transmitted signals at T0, T1…T7, and reflections at A, B…F are discussed in the text. T0: 25.5ns; T1: ~2.4ns; T2: 31.5ns; T3: 37.0ns; T5: 76.2(78.0)ns; T6: 82.6ns; T7: 88.4ns. A: ~0ns, B: 51.0(52.0)ns; C_1: 23.3ns; C_2: 27.6ns; D: 5.5ns; E: 45.7ns; F: 56.9ns. The time resolution is 0.122 ns.

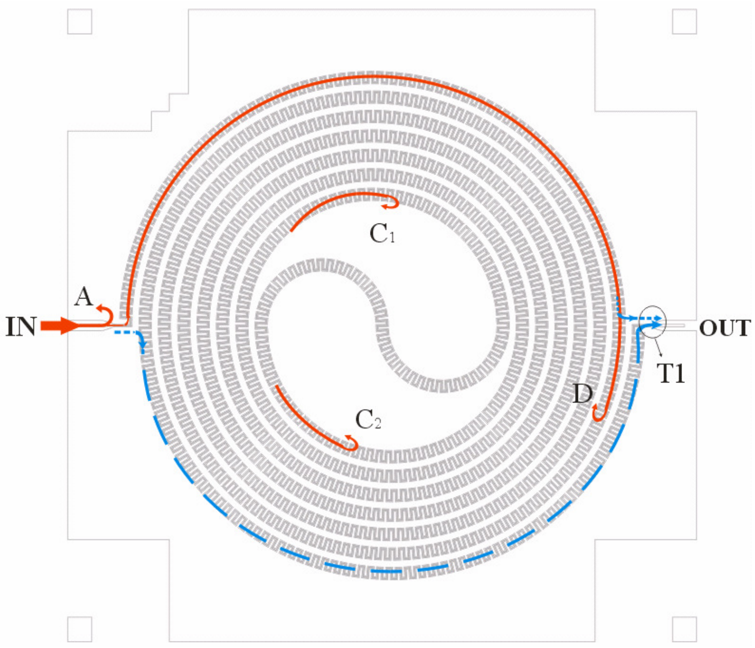

Figure 9.10 Illustration of the reflections (A, C_1, C_2, D) and backward coupling (T1) in the double-spiral meander line structure. See the text for details.

Figure 9.9(b) includes the reflection responses of an impulse band-limited between 2 and 18 GHz. A symmetric pattern centred at 25.5 ns is shown from 0 to 51 ns. This implies that the main reflecting elements are the input/output (peaks A and B) and the inner part of the spirals (C_1 and C_2). It is also important to note that the responses seen from both ports (S_{11} and S_{22}) are in reasonable agreement with each other. This indicates the main features in the reflection response are not because of defects in the superconductor circuit or dielectric substrate, as they are most unlikely to be distributed symmetrically. The first peak (A) is reflected from the feed-line area at the input, as illustrated in Figure 9.10. Its magnitude is less than -20 dB. The peak B is reflected from the feed-line at the output after the signal travels all the way through the delay line. It is delayed by twice the transit time of signal T0. The pair of peaks C_1 and C_2 are reflected from the inner part, but not exactly the middle, of the spirals. Both peaks are 1.1 ns (one way transit time) away from the middle point at 25.5 ns. The spots of the reflections in the delay line are marked in Figure 9.10.

Another reflection peak at ~5.5 ns (D) is consistent with a signal path from the input, along a semi-circle on the outermost turn, a reflection due to the proximity of the output terminal, and back along the same path as shown in Figure 9.10. This reflection causes the 180 MHz ripple period in Figure 9.6(b). Peak E is 5.3 ns before B. It may be the counterpart of D and reflected when the signal is on the outermost semi-circle leading to the output port. Both D and E stand out in S_{22}. However, E in S_{11}, which should correspond to D in S_{22}, is not present. The reason is not clear. Peak F is 5.9 ns later than B and it may be delayed due to multiple reflections at the discontinuity causing D. The peaks T2 and T3 in the transmission response are very likely to be delayed by similar multiple reflections. The above analysis presents strong indication that the discontinuity that results in D is another important reflecting element. According to the delay time, it can be located in the area, where the feed-line of one port meets the outmost semi-circle leading to the other port, as shown in Figure 9.10. The origin of such reflections is not yet fully understood. However, the structures causing D and C_1, C_2 seem to share some similarity in their proximities. They are the regions where the meander line carrying the signal experiences a transit from being accompanied by meander lines on both sides to being accompanied by a meander line only on one side. This may result in a discontinuity.

The cluster of peaks at T4 is caused by the multiple reflections from the inner part of the spiral. T5, T6, and T7 are ~51 ns later than T0, T2, and T3, respectively, due to the multiple reflections between the input and output ports.

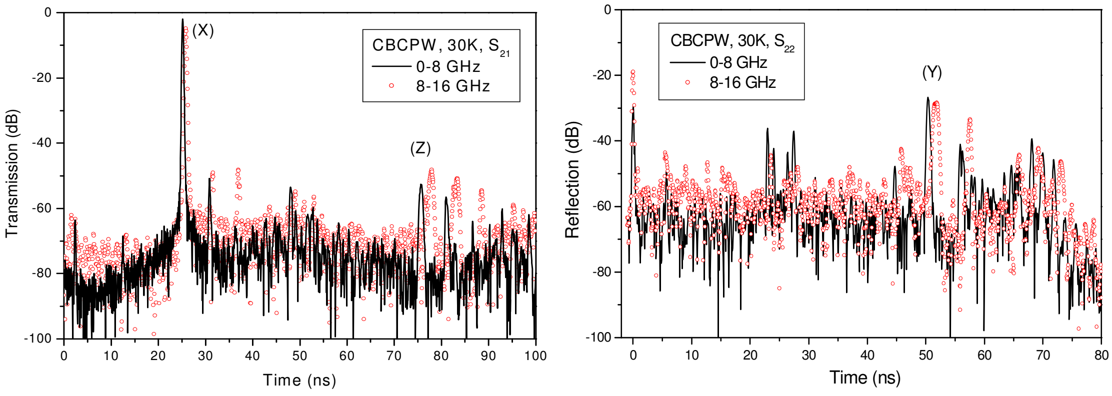

(a) (b)

Figure 9.11 Time domain responses for impulses band-limited to different frequency ranges (0-8 GHz and 8-16 GHz).

The time responses of the CBCPW delay line in Figure 9.9 are from an input impulse containing the entire passband from 2 to 18 GHz. It is also interesting to differentiate the contributions from different bands. Figure 9.11 shows the time responses of 0-8 GHz and 8-16 GHz. Over the band of 8-16 GHz, the signals are delayed by slightly longer time, which is the result of dispersed velocities at different frequencies. As expected, the time differences of the transmission/reflection peaks are proportional to their delay time, which is 0.7 ns for peak-X at ~25ns, 1.5 ns for peak-Y at ~51 ns, and 2.3 ns for peak-Z at ~76 ns. Normally, the dispersion widens the signal as in the case of T0. However, for Y and Z, the dispersion splits the signals B and T5 in Figure 9.9. One possible reason is that the reflections producing B and T5 are localised to certain bands in the frequency domain. In addition, the reflection A (Figure 9.9) is reduced from -20 dB to less than -30 dB for the band of 0-8 GHz, as shown in Figure 9.11(b). The signal T1 at ~2.4 ns can be recognised more easily in Figure 9.11(a).

9.3.2 Time responses for feed-line areas

The quality of the transition and connection in the feed-line area is also examined by time domain measurements. In order to have a better time resolution, the “low-pass” transformation mode[6] is used, with a band limited between 0.05 and 20.05 GHz. As calculated in Table 9-1, this gives a resolution of 49 ps. The inverse Fourier transform based on this mode only results in real parts, which can be interpreted as the reflection coefficient ρ ($0 \leq |\rho| \leq 1$). This “low-pass” mode simulates the time-domain-reflectometry (TDR) measurement. It could be used to identify the types of the discontinuities (inductive, capacitive, resistive, etc.).[6,7,8] It should be pointed out that a correction of 0.016 ns is applied here on the measured reflection responses due to the use of the non-standard calibration kit (SMA-short), as addressed in Section 7.3.

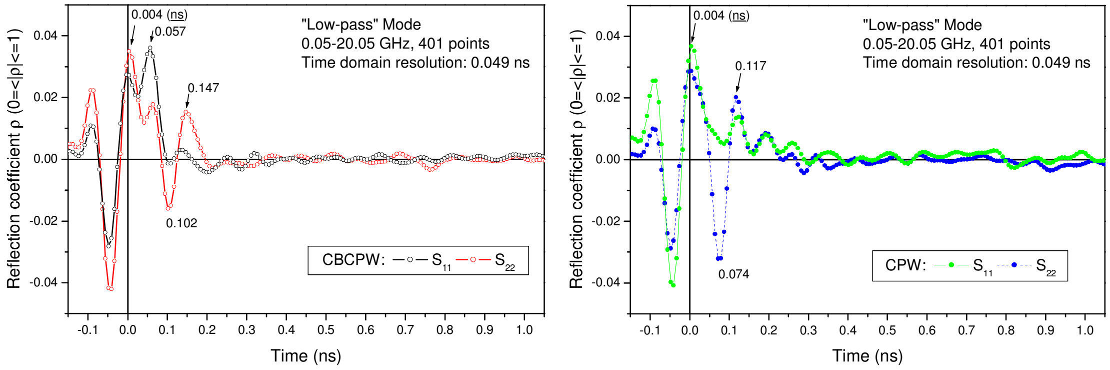

(a) (b)

Figure 9.12 The time domain reflections in the feed-line areas of (a) the CBCPW delay line and (b) the CPW delay line. The shown delay times are corrected, which are 0.016 ns less than the measurement readings.

Figure 9.12 shows the measured reflection coefficients seen from both ports (S_{11} and S_{22}). The first few peaks after the zero time are reflections from the feed-line area with the contributions from the transition and connection discussed in Chapter 6. For the CPW delay line, the transition is a CPW-type tapering, while for the CBCPW delay line it is a CPW-to-CBCPW transit. Both transitions are connected to K-connectors with silver-loaded epoxy. The reflection coefficients of both delay lines are less than 0.04, indicating good transmission efficiency. It should be mentioned that the position of the time zero is subject to small uncertainty. It is somewhere inside the coaxial K-connector before its contact point with the superconducting circuit.

In Figure 9.12, the first reflection peak close to the time zero at 0.004 ns should be related to the mating interface between the SMA-plug and the female K-connector. With different dielectric media (PTFE for SMA versus air for K), the connection interface is discontinuous. It would be better if connectors of the same series were used, such as K-plug to K-jack. The peaks thereafter may be reflected at the contact point between the K-connector and the superconducting circuit, then the tapering transition and the first bend structure of the meandered delay line. The 0.057 ns peak for the CBCPW delay line corresponds to a length of ~9 mm in free space, close to the length of the K-connector (10.3 mm). It is considered as the end of the transmission inside the K-connector and may be reflected due to the discontinuity at the contact point of epoxy. The peaks beyond this should be those reflected from the superconducting circuit and travels in a velocity of ~85.7 mm/ns (for a coplanar line with $LaAlO_3$ substrate). From the epoxy contact to the first bend structure of the meander delay line, the distance is about 4 mm (~0.047 ns signal delay). So it takes another 0.094 ns for the signal to be reflected on entering the mender line. Because the adjacent bends in the meander line are only separated by 0.84 mm (0.01 ns signal delay), the consecutive reflections from them cannot be resolved. However, the small fluctuation beyond 0.2 ns in Figure 9.12 should be related to the periodic change of the input impedance down the meander structure. Curved or mitred bends could compensate the discontinuities and achieve a better matched meander line.

9.4 Box modes

One particular problem for a wideband device is the box modes. These modes come down in frequency as the size of the packaged device increases, and could compromise the transmission efficiency if they couple significantly to the circuit. For a delay line, the package size is necessarily large as a long delay time is required, so box modes often present a problem. Experimentally, the box modes in a superconducting device can be observed when the temperature is above T_c.

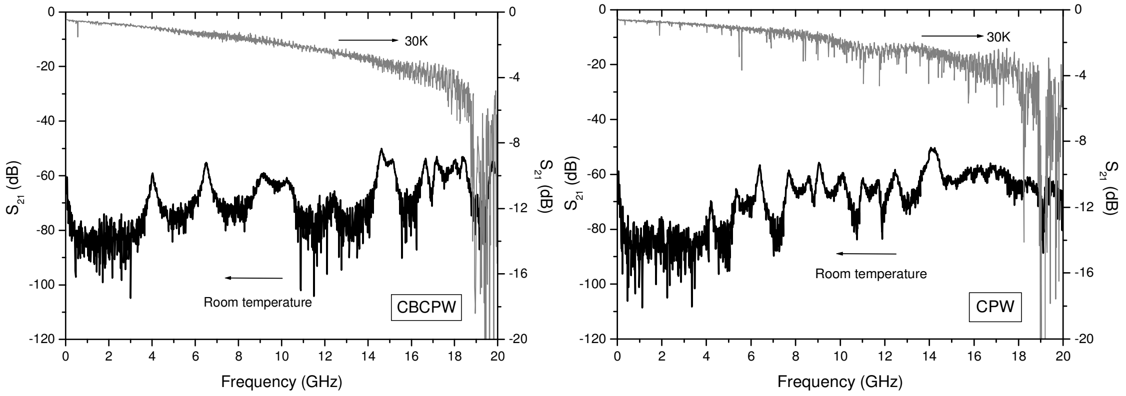

(a) (b)

Figure 9.13 Box modes (package modes) of the CPW and CBCPW delay lines

If the packaged HTS device is measured at room temperature, there is neither transmission nor resonance through the superconductor delay line, so the observable resonances should be the modes of the metal box, loaded with a substrate but without conducting circuit on it. Figure 9.13 shows the measurements at room temperature and 30K. The observed box modes are less than -50 dB for both delay lines. However, there is no evidence of the consequences at 30K for the CBCPW delay line as shown in Figure 9.13(a). For the CPW delay line, the effect of box modes at 30K is almost unrecognisable from Figure 9.13(b) and may be seen more easily in Figure 9.14 at around 14 GHz.

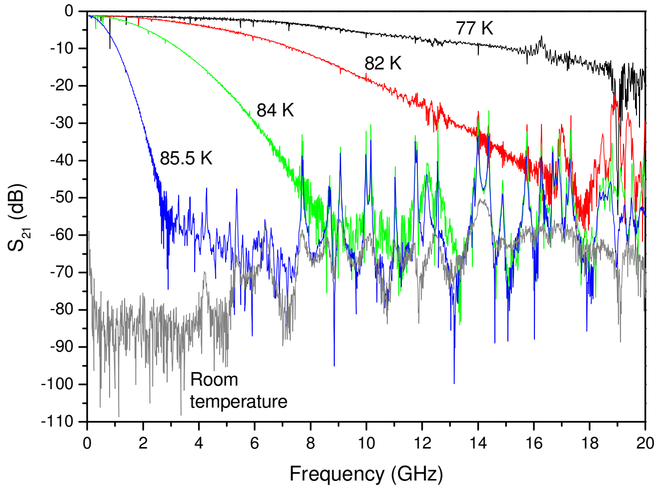

Figure 9.14 Change of the S_{21} response at temperatures close to the superconducting transition. The measurements are taken on the CPW delay line, with the epoxy contacts re-made after the measurements of Figure 9.1. The frequency step is 12.5 MHz.

Figure 9.14 shows the evolution of the S_{21} response as the CPW delay line is warmed up from 77K to room temperature. The transmission response is gradually dominated by resonant peaks emerging initially at the high frequencies, as can be seen from the graphs for 82, 84, and 85.5 K. The resonances at these temperatures seem to have some correlations with the box modes at room temperature, but much stronger in magnitude. At temperatures close to the superconducting transition T_c, although the conductivity becomes poor, the current on the delay line may not die out completely, which helps excite stronger box resonances. The substrate plays an important role on the induction of box modes. Without the $LaAlO_3$ substrate, there are hardly any observable box resonances between 2 and 20 GHz. Several configurations illustrated in Figure 9.15 have been used to look into the box modes in the coplanar delay lines.

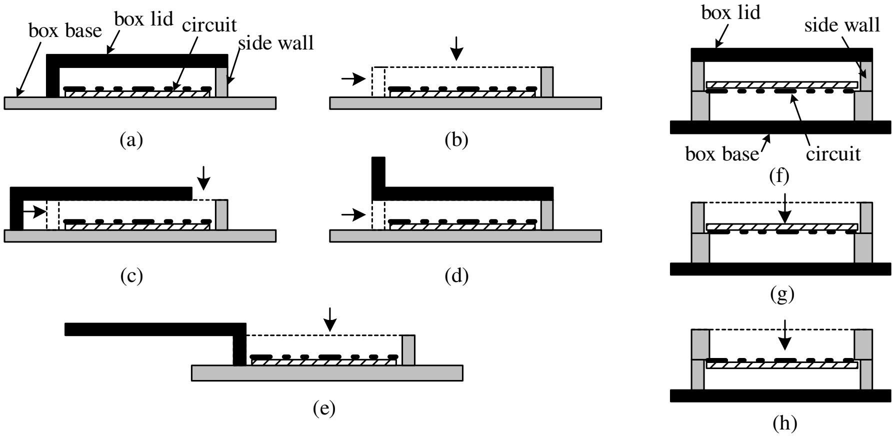

Figure 9.15 Configurations used to look into the box modes. The arrows point to the surfaces that are open to air. Configurations (a)-(e) are for the CBCPW delay line, (f)-(h) for the CPW delay line. The input and output are perpendicular to the page.

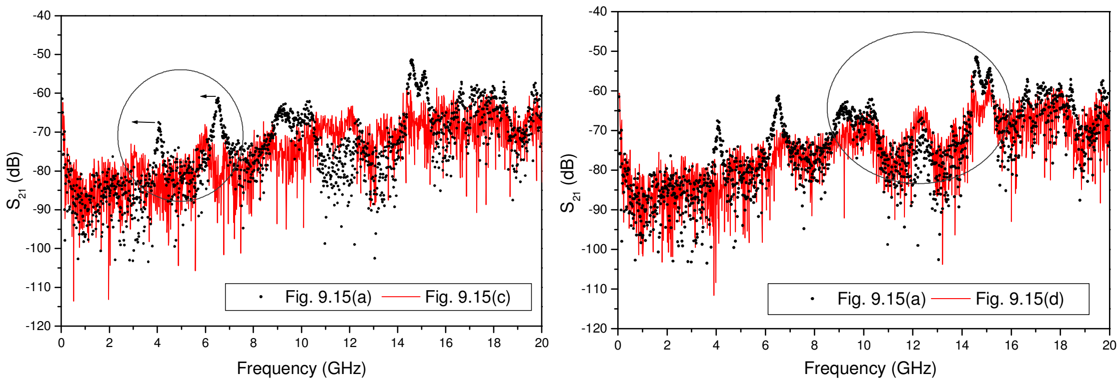

(a) (b)

Figure 9.16 The change of box modes in the CBCPW delay lines with different configurations as shown in Figure 9.15(a)-(e).

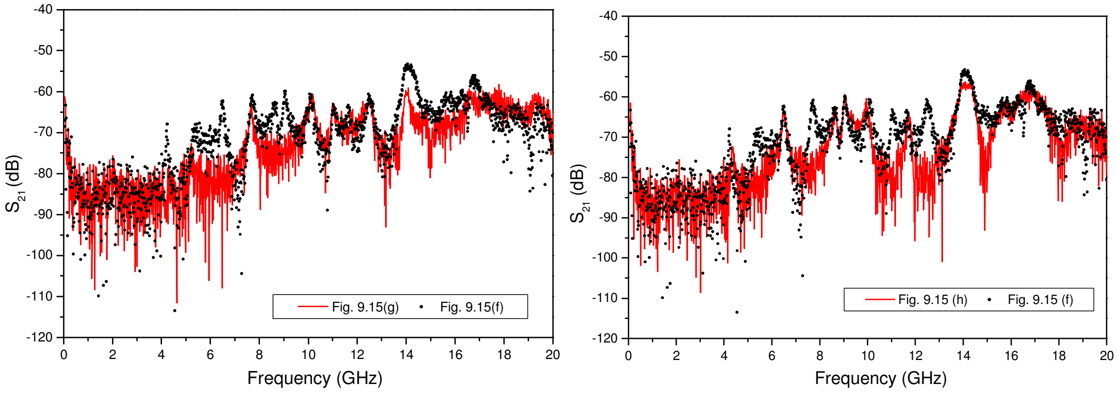

(a) (b)

Figure 9.17 The change of box modes in the CPW delay lines with different configurations as shown in Figure 9.15(f)-(h).

For the CBCPW delay line, Figure 9.15(a) is the package in a normal position. If the L-shape box lid is displaced as Figure 9.15(c), all box modes are reduced, and particularly the two resonances below 8 GHz appear to shift to lower frequency as shown in Figure 9.16(a). In contrast, with the configuration of Figure 9.15(d), both resonances disappear while the resonances above 8 GHz are still recognisable in Figure 9.16(b). These may imply that the two modes below 8 GHz are more relevant to resonances between the side-walls. If the circuit is open to air as in Figure 9.15(b, e), all resonance peaks disappear except the one at the low-frequency end, which may be attributed to RF leakage. Unlike the CBCPW delay line, removing one of the shields (Figure 9.15(g, h)) of the CPW delay line does not eliminate all the resonances, as shown in Figure 9.17. Some of the resonances are induced in the cavities above or below the circuit independently.

For both coplanar delay lines, the box modes are so weak that their effect on the transmission responses is insignificant. However, for a microstrip-type delay line packaged in a box of similar size, some box modes are higher than -40 dB, which did result in spurious transmission dips in the responses at superconducting temperatures (Fig. 7 of reference [9]). To reduce the effect of box modes, one approach is to drive them out of the band of interest by decreasing the chamber volume of the package. As some box modes seem relevant to the resonance between the side-walls, the width of the box has to be reduced, which is difficult to achieve for a long delay line. Another approach is to lower the magnitude of box resonances. Slightly increasing the conductor loss of the side-walls might work in terms of reducing the *Q* of box resonance, but this has be controlled before it adversely increases the transmission loss of the circuit.

9.5 Radiation

By removing the box lid as in Figure 9.15(b, h) and looking for changes in the transmission responses at superconducting temperatures, the effect of radiation was estimated. For the CBCPW delay line, the changes are very small up to 16 GHz and can only be observed when the frequency approaches 19 GHz, where the resonance occurs. For the CPW delay line, Figure 9.18 shows the differences of S_{21} between the device with either the box lid or base removed (Figure 9.15(g, h)) and a fully packaged one (Figure 9.15(f)). Generally, ΔS_{21} is negative and small, showing the radiation slightly increases the transmission losses. Unexpectedly, there is a concave of 1 dB between 8 and 13 GHz. In this frequency range, the packaged CPW delay line also shows exceptionally lower S_{21}, as can be seen from Figure 9.1 or Figure 9.3(b). The origin for this is not yet known. The positive values of ΔS_{21} at a few scattered frequencies are most likely to be related to the eliminations of box resonance when the device is opened to air. But there is no good correlation with the box resonances in Figure 9.13(b), except at 9 and 14 GHz.

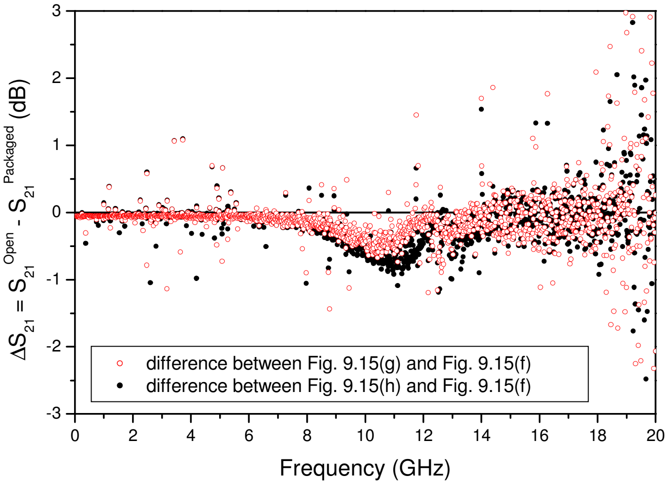

Figure 9.18 The change of S_{21} at 30K when the CPW delay line is opened to air on the surface of YBCO circuit (Figure 9.15(h)) or the bare substrate (Figure 9.15(g)).

9.6 Measurement uncertainty

There are some factors that may affect the accuracy in measuring the delay lines. Firstly, the quality of the microwave cable-assemblies, interconnecting the device with the measurement system, plays an important role. About 2.8 m cables are used, including two 1m-long flexible cables connecting the analyser to the hermetic adaptors on the wall of cryostat, and two 40cm-long semi-rigid cables (inside the cryostat) connecting to the device under test. Losses of the cables and reflections due to the mismatch between connectors/adaptors are inevitable. However, as long as the values of the losses and reflections are stable, calibration can normally eliminate their effect on the measurement results of the delay lines. By experience, unstable interconnections could invalidate the calibration and add their own contributions to the S_{21} response. Semi-rigid cables are more immune to the vibrations and movements than flexible cables and able to maintain a steady performance. The optimal operation frequency of the cable assemblies is limited by the SMA-connectors and RG405 semi-rigid cables, which have specified operation frequencies below 18 GHz. The repeatability of the calibrations at frequencies higher than 20 GHz is not as good as below 20 GHz. However, except between 24 and 28 GHz (as discussed in Section 9.2.5), there is no evidence showing that the cable assemblies contribute to the features of the measured responses. The reasonable agreement of S_{21} between different runs of cryogenic measurements is a proof. If the effects of the assemblies are not well calibrated or their performances are unstable, the responses from different runs are expected to differ from each other.

Secondly, as a non-standard adaptor is used for the low-temperature calibration of S_{21}, the transmission efficiency of the adaptor itself may also have an impact on the measurement. Ideally, the adaptor should have zero electrical delay and must have a wide operation frequency range free from resonance. In this work, a K-type adaptor with an operation frequency up to 40 GHz is used, well covering the band of interest. But it has an electrical delay of ~0.05 ns. This has been offset in the calibration process. In the worst case, it may cause a small error in the time delay by 0.05 ns.

As mentioned before, the excessive resistance of the conducting epoxy can add its contribution to the measured insertion losses. As shown in Figure 9.19(a), S_{21} does have some correlation with the DC resistance of the epoxy, which was measured using a digital multimeter. The transmission coefficient S_{21}, corresponding to an additional DC resistance of R_{dc}, can be given by

$$S_{21} = 20\log\left(\frac{2}{2+R_{dc}/Z_0}\right) = 20\log\left(\frac{1}{1+R_{dc}/(100\Omega)}\right) \qquad \textbf{Equation 9-1}$$

According to (9-1), the resistances of 3.2, 13.5, 44.2 Ω result in -0.27, -1.1, and -3.2 dB in S_{21}, which agree very well with the measured S_{21} at the low-frequency end in Figure 9.19(a). In the time domain, the reflection peak at 0.094 ns in Figure 9.19(b) may be well related to the excessive resistance of 13.5Ω. This resistive loss can be avoided, if the epoxy is cured under the optimal condition.

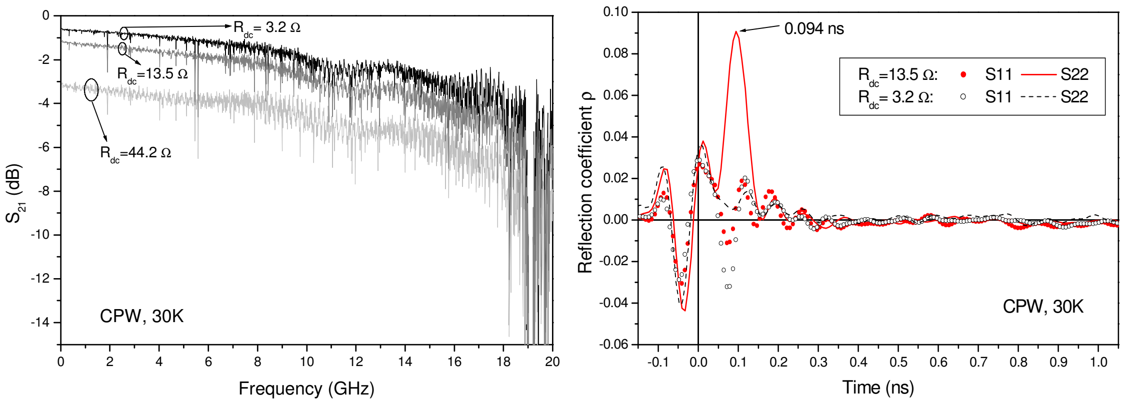

(a) (b)

Figure 9.19 Variation of the measured (a) transmission responses and (b) time domain reflections, as the DC resistance of the epoxy changes. (The shown delay times are corrected, which are 0.016 ns less than the measurement readings.) R_{dc} corresponds to the DC resistance of the epoxy used at both ports.

It is also worth mentioning that the low-temperature calibration process used in this work is not the highest accuracy as can be achieved for room temperature and narrow band measurements using a full 2-port correction[6]. The low-temperature calibration is basically a "response" calibration. There have been difficulties in pursuing full 2-port calibration for the wideband delay lines operating at low temperatures. First of all, the standard calibration kits are not for use at superconducting temperatures. To perform low temperature calibration, non-standard kits, such as coaxial adaptor and short, have to be used. A TRL (thru-reflect-line) calibration set based on planar transmission lines may be a better choice for higher-accuracy, wideband, and low-temperature. Secondly, although one may take measurements at 30K based on full 2-port calibration at room temperature and do the correction afterward, the amount of correction is difficult to determine accurately over a wide frequency range. It is believed that such corrections are only suitable for very narrow band measurements.

9.7 *Power dependence*

Planar superconducting devices usually have poor power handling due to the nonlinearity of superconductors. The nonlinearity can manifest as increased surface resistance with power, or intermodulation where new frequency components not in the original signal can be generated and cause distortion. Intermodulation is more of a problem in a resonant structure, as the input power is amplified inside the resonator. For a delay line, this should not be a serious problem unless the incoming signal is at a high power level. Here, only the effect of increased loss with power will be looked into.

The power dependence of the delay lines is investigated at 2, 10, and 18 GHz and at different temperatures. Figure 9.20 shows the S_{21} values of the CPW and CBCPW delay lines plotted against the input power to the device under test. The same experimental arrangement as in Figure 8.17 is used. Room temperature calibration is adopted in this set of measurements, which only affects the readings of S_{21} without changing the profile of its power dependence.

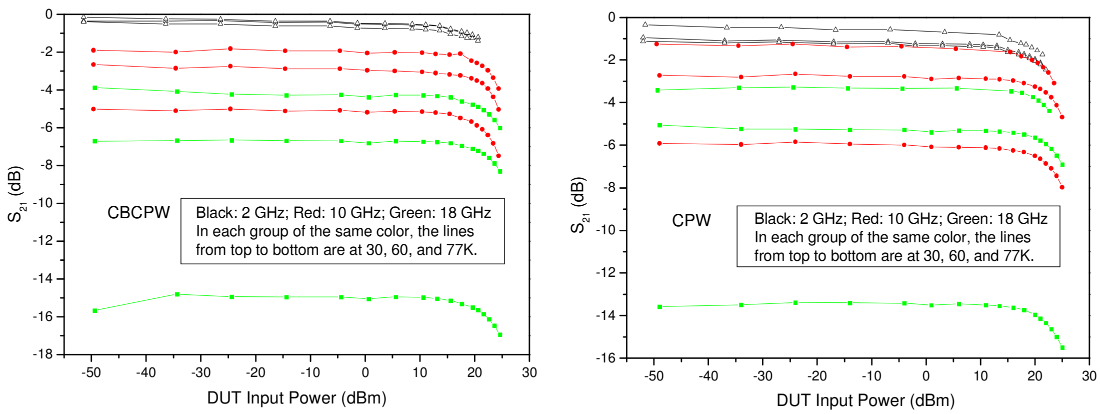

Figure 9.20 Change of the measured S_{21} values at 2, 10, and 18 GHz with the input power to the delay lines. (Room temperature calibration is used in this set of measurements.)

Up to the measurement limit of 25 dBm, the CBCPW delay line shows similar power dependence to the CPW line. The measured S_{21} only varies slightly when the input power is less than 15 dBm (0.032W), and decreases faster at above 15 dBm as the nonlinearity of the superconductor becomes important. It appears that this “transition” power, at which S_{21} starts to decrease rapidly, does not change much with temperature and frequency. However, this does not mean the superconductors follow the same power-dependence at different temperatures and frequencies. Due to the attenuation of the delay line, the power in the superconductor decays spatially along the wave propagating direction. The power at different points along the superconductor line will not be constant. Therefore, it is not straightforward to study the power dependence of the superconductor using a delay line.

9.8 Summary

Both coplanar delay lines have been measured at 30, 60, and 77K. Without using any bond-wires to join the two in-plane grounds, the delay line based on the CBCPW shows excellent transmission performance, free of resonance over a wide frequency band from 2 to 18 GHz. Compared with other previous work in Table 2-1, the performance of this delay line is the world's best in terms of its widest transmission band (2 to 18 GHz), low transmission loss (0.06 dB/ns at 60 K and 10 GHz), small ripple (<1 dB up until 16 GHz), and small dispersion (< 2 ns in the variation of group delay between 2 and 18 GHz). This is also the first coplanar delay line successfully demonstrated without using wire-bonding.

The main findings in this chapter are:

(1) With the conductor backing, the CBCPW delay line effectively suppresses the spurious modes and achieves a wide band free from resonance from 2 to 18 GHz. The operation of the conductor backing may be explained as a "wireless" interconnection of the in-plane grounds through the capacitance between the upper and lower ground planes. The effect of the conductor backing on the parasitic modes in a wider application context is worthy of further investigation.

(2) In terms of variation of group delay with frequency, the delay lines disperse by 2 ns (out of 25 ns total delay) between 2 and 18 GHz. The CBCPW delay line has smaller dispersion and slightly longer delay. The difference in the group delay between the CBCPW and CPW decreases and eventually disappears at high frequencies. This indicates the conductor backing has more influence on the field distribution in the lower frequency band. It is also found that the group delay and dispersion of the experimental delay lines can be accurately predicted by simulating a short section of unwound meander line.

(3) The bandgap at 19 GHz predicted by the full-wave simulations is confirmed

experimentally, which is the upper limit of the achievable bandwidth of the coplanar DSML delay line.

(4) The time domain measurements show that the reflecting elements in the DSML structure are the feed-line areas at the input/output, the inner part of the spiral, and the area where the feed-line of one port meets the outmost semi-circle leading to the other port of the meander line.

(5) From the time-domain reflection measurement, the quality of the transition and connection in the feed-line area is examined, giving a reflection coefficient of 0.04. The unwanted resistive loss of the epoxy connecting the sliding contact with the delay line causes some excess insertion loss.

(6) The box resonances are less than -50 dB, observed at the room temperature. But there is no consequence at the superconducting temperatures in the transmission response of the delay lines.

(7) The insertion losses of the delay lines only change slightly at different input-power levels less than 15dBm. The “transition” power, at which S_{21} of the delay lines starts to decrease rapidly, does not change much with temperature and frequency.

Comparison with a DSML microstrip delay line[9]:

In parallel with the coplanar delay lines reported in this thesis, a microstrip version of the DSML delay lines[9] is also tested within the same project. As expected, the microstrip delay line gives slightly lower loss per unit delay. The microstrip delay line is very dispersive due to a tight coupling (equal line and gap widths) between the meander segments. The measured group delay is 29 ns at 0.05 GHz, and increases by more than 100% to 73 ns at 20 GHz. It effectively becomes a fast-wave structure at low frequencies. As shown in Fig. 4 of reference [9], the travelling wave in the meander line is about 1.75 times faster than in a straight line (~0.6 ns versus ~1.05 ns delay at the low end). Similar simulation shows the coplanar meander line only speeds up the wave by a factor of 1.06. This difference may also contribute to the different influences of box resonances in the experimental devices. Box resonances are clearly identified as transmission notches in the measured microstrip device, but not in either of the coplanar devices. The propagation mode in the microstrip delay line may be more easily coupled to the box mode, as its velocity is closer to the free-space velocity than the coplanar devices.

---

[1] G. J. Hofer, H. A. Kratz, G. Schultz, J. Sollner, V. Windte, "High temperature superconductor coplanar delay lines," *IEEE Trans. Appl. Supercond.*, vol. 3, no. 1, pp. 2800-2803, Mar. 1993.

[2] G. K. G. Hohenwarter, E. K. Track, R. E. Drake, R. Patt, "Forty five nanoseconds superconducting delay lines," *IEEE Trans. Appl. Supercond.*, vol. 3, no. 1, pp. 2804-2807, Mar. 1993.

[3] N. Fenzi, D. Aidnik, D. Skoglund, S. Rohlfing, "Development of high temperature superconducting 100 nanosecond delay line", in *High-T_c microwave superconductors and applications*, Robert B. Hammond, Richard S. Withers, Editors, Proc. SPIE 2156, pp. 143-151 (1994).

[4] A. A. Omar, Y. L. Chow, "Coplanar waveguide with top and bottom shields in place of air-bridges", *IEEE Trans. Microwave Theory Tech.*, vol. 41, no. 9, pp. 1559-1563, Sep. 1993.

[5] S. H. Talisa, M. A. Janocko, D. J. Meier, C. Moskowitz, R. L. Grassel, J. Talvacchio, P. LePage, D. C. Buck, R. S. Nye, S. J. Pieseski, G. R. Wagner, "High-temperature superconducting wide band delay lines," *IEEE Trans. Appl. Supercond.*, vol. 5, no. 2, pp. 2291-2294, Jun. 1995.

[6] User's Guide of 8719ET/20ET/22ET/19ES/20ES/22ES Network Analyzers, Agilent Technologies, Inc., June 2002.

[7] R. E. Collin, *Foundations for microwave engineering*, 2nd ed., McGraw-Hill, 1992, pp. 78-85.

[8] C. W. Davidson, *Transmission lines for communications*, 2nd ed., Macmillan Education, 1989, pp. 92-98.

[9] H. T. Su, Y. Wang, F. Huang, M. J. Lancaster, "Wideband superconducting microstrip delay line", *IEEE Trans. Microwave Theory Tech.*, vol. 52, no. 11, pp. 2482-2487, Nov. 2004.

Chapter 10 Conclusions

10.1 Summary

Two 25 ns wideband HTS delay lines with a novel double-spiral meander line (DSML) structure are designed, fabricated and measured. One is based on the conventional CPW line, and the other based on a conductor-backed coplanar line (CBCPW). The design relies mainly on full-wave simulations and conformal-mapping calculations. Transmission-line parameters, such as characteristic impedance, loss, and cross coupling as a function of geometric dimensions are evaluated as a basis for the device design. The device design focuses on the selection and optimisation of the routing pattern of the delay line. It involves the considerations of trade-offs between the size and performance, such as loss, bandwidth, dispersion and delay time. The wideband transitions from narrow to wide transmission lines and the connections with external coaxial connectors are designed separately from the main circuit. The measurements of the delay lines are taken in two stages. The first stage is to characterise the delay line as a resonator. The surface resistances of the superconductors and the temperature- and power-dependent properties are investigated by measuring the Q-values of more than 1000 harmonics from 20 MHz to 20 GHz. In the second stage, the delay line is fully connected as it would be used in the application. The bandwidth, insertion loss, ripples, dispersion, and delays are the most important parameters measured. The results from this measurement are compared comprehensively with those from both resonance measurement and simulations. The reflecting elements in the DSML structure are identified by the time-domain analyses.

10.2 Conclusions

The performance of the CBCPW delay line is the best ever demonstrated in terms of the widest resonance-free band (2 to 18 GHz), low insertion loss (0.06 dB/ns at 60 K and 10 GHz), small ripple (<1 dB up until 16 GHz), and small dispersion (< 2 ns in the variation of group delay between 2 and 18 GHz). This is the first coplanar delay line successfully demonstrated without using wire-bonding. This thesis also presents a systematic design of the HTS delay lines and an approach to characterise the material properties using coplanar resonator techniques over a wide and continuous frequency band.

Application prospect

The implemented CBCPW-type delay line generally meets the project specification very well. It can be used to provide a real time delay of 25 ns on 2-in wafer over a wideband between 2-18 GHz free from resonances. There is still room for the bandwidth to be extended to 21 GHz without sacrificing the use of wafer area. The delay capacity can be enhanced to 70 ns if the same design is adopted on a wafer of 3-in in diameter. Such $LaAlO_3$ wafers are commercially available.

To achieve the specified insertion loss of no more than ~8 dB per 50 ns (~0.16 dB/ns), the delay line has to be operating at below 60 K. At 60K, the superconducting CBCPW delay line is able to give a reasonably low insertion loss of 0.2 dB/ns at 18 GHz. This is estimated from the resonance measurements, avoiding the effects of the connections, and can be used to assess the loss of the superconducting delay line itself. The experimental result from the transmission measurements is higher than this. At 60K, the measured S_{21} is less than 6dB (0.24 dB/ns) at the upper band limit of 18 GHz. As pointed out in Section 9.2.2, this includes 1-2 dB loss due to the excess resistance of the epoxy, which is avoidable so long as the epoxy is optimally cured. A straightforward way to reduce the loss is to increase the conductor width, but at the cost of the substrate area. This is feasible if a bigger circuit size can be tolerated. It is also important to note that the quality of the patterning plays a role in the loss level. Practically, the slightly narrower coplanar line, due to over-etching, increases the current density and brings more conductor loss.

The main factor limiting the performance is the mismatches at the neighborhood of the feed-lines and the large number of bends along the meander line. This could have increased the magnitude ripple, phase ripple, and reflection loss. In the feed-line areas, the main reflecting elements are the input transitions and the areas where the feed-line of one port meets the outmost semi-circle leading to the other port. These bring unwanted signals lagging behind the main transit pulse, as can be seen in time-domain responses. This could possibly trigger wrong responses if used in electronic warfare and radar systems, especially as the incoming signal is strong. To improve it, the feed-line areas should be further optimised using full-wave simulations. Compared with a smooth transmission-line structure, such as a double-spiral line (DSL), the DSML structure has extra loss due to the reflections and current crowding at the large number of bends. Mitred or curved bends should be a better choice.

The recipient system of this delay line should be able to tolerate small ripple and dispersion. My design aims to minimise the ripple and fully understand the origin of the dispersion so as to predict it accurately. The measured ripple is less than 1 dB up until 16 GHz, which is good, compared with other work on superconducting delay lines. This ripple increases faster as the frequency approaches the bandgap at 19 GHz. It can be reduced, if the bandgap is pushed to higher frequencies, which can be achieved by shortening the coupled length in the meander structure. It can be further lowered by improving the match at the input/output and bends. The dispersion of the DSML delay line is mainly determined by the coupling between the short meander segments, and almost unaffected by the coupling between the spiral-turns. This makes it possible to predict with a high accuracy the dispersion by simulating a short section of unwound meander line.

About the DSML delay line structure

The achievable bandwidth of the coplanar DSML structure is limited by a bandgap due to the quarter-wavelength resonance on the in-plane ground fingers of the meander line. This bandgap is a unique feature for a coplanar meander line because of the presence of finite in-plane grounds. It is predicted by simulations and proven in the measurement.

The DSML structure is not very efficient in using the central area of the substrate as sufficient space is needed to maintain a proper meandering pattern. Though, it is feasible to reduce the coupled length (l_c) of the meander in the inner part of the spirals, and fit in a longer delay without sacrificing the bandwidth. A major advantage of the DSML structure is that it reduces the forward coupling present in the conventional double-spiral structure, which is normally cumulative with length. According to the simulation results in both the frequency and time domain, the DSML shows much better transmission properties than the DSL over a wide frequency range up to 18 GHz.

About CPW and CBCPW

The CPW and CBCPW, of the same dimensions, are compared with each other in every aspect of the design and measurement. The CBCPW line is slightly lossier than the CPW. However, a lower cross-coupling is shown between a pair of CBCPW lines, slightly reducing the dispersion of the CBCPW meander structure. The difference of the group delay between the two coplanar delay lines decreases as the frequency goes higher and eventually disappears. This indicates the conductor backing of the CBCPW has more influence on the field distribution at lower frequencies. One of the main findings in this work is the S_{21} response of the CBCPW delay line is free from spurious resonances over a wide bandwidth without using any wire-bonds, whereas the CPW delay line suffers from many transmission notches. The resonance measurements also show distinct anomalies between the two coplanar lines in the Q-graphs as a function of frequency, suggesting different mechanisms of parasitic modes. For the CBCPW line resonator, some anomalous dips in the Q-graphs are caused by package modes, while others may be related to parallel-plate modes. For the CPW resonator, the anomalous Q-values most likely result from the interference between dominant coplanar mode and parasitic slotline mode. The notches in the S_{21} responses of the CPW delay line should be attributed to the same reason.

A problem with the CBCPW structure is the possible induction of microstrip-like mode, especially for a wide coplanar line with a slot width comparable to the substrate thickness. This is not the case for the main part of the delay line. However, in the feed-line area where the narrow delay line tapers to a much wider external connector, the parasitic microstrip mode does present a problem. This makes it difficult for a CBCPW-type taper (transition from 0.2 mm to 0.04 mm) to achieve a wide bandwidth. Two other transition structures are therefore designed. One is the CBCPW-to-microstrip transition utilising the mode conversion, the other is a CBCPW-to-CPW transition avoiding the microstrip mode. The bandwidth of the first design cannot cover 18 GHz unless the CBCPW in-plane ground and the microstrip lower ground are interconnected by vias. This design is abandoned in the experimental devices considering the fabrication difficulty. The second design is successfully implemented in the CBCPW delay line. Unlike the CBCPW, the transition for the CPW delay line is easily achieved by a CPW-type taper. However, the packaging of the CPW delay line is more challenging, because only the wafer edge has direct contact with the box (ground) in a flip-chip configuration, leaving cavities both above and below the substrate. In this work, the wafer is mounted solely by adhesive conducting-film without using springs. Good mechanical strength is maintained during many cooling cycles.

About methodology

Various analytical methods and full-wave simulators are used in the design. The transmission-line parameters of both CPW and CBCPW, such as characteristic impedance, loss, and coupling, are evaluated by conformal mapping and compared with simulation results. Using the simulation as a benchmark, the conformal mapping technique yields satisfactory accuracy in calculating these characteristic parameters. The dispersion and bandwidth of the coplanar meander lines are investigated using Sonnet. The results are in good agreement with experiments. The difficulty in simulating a large-scale and complex coplanar circuit, as the DSML delay line, is overcome by adopting the slot-layer simulation technique provided by ADS. The same length of DSML and DSL are compared using this method. The transition and connection between the coplanar line and coaxial connector are simulated using HFSS with 3D modelling capability.

The conductor loss of the HTS coplanar waveguide is an important parameter. It is evaluated using Holloway's approach, taking the magnetic penetration in superconductors into account. Temperature-dependent geometric-factors are derived to establish the relation between the attenuation and surface resistance. Other two formulas originally for normal conductors are also considered, based on the incremental-inductance method and the current-density method respectively. The former is adopted to derive an analytical expression for the loss of the CBCPW, in order to account for the loss increase due to the conductor backing. This increase is only 2% for the coplanar lines used in this work.

About the device and material characterisation

The measurements based on the resonator technique provide useful information on the delay-line devices and the HTS materials as well. The attenuation acquired in this way excludes the effect of connection loss, so it sets the lower limit of the achievable insertion loss for the delay lines. The surface resistance of the superconductor is determined over a wide and continuous band from 20 MHz to 20 GHz by measuring the Q-values of more than 1000 harmonics of the delay-line resonators. The results do not give a profile of f^2-dependence. At the low frequency end, it is more like a linear dependence. Both experimental errors in measuring Q-values and the deficiency of the transmission-line model used to formulate GF_c could have affected the accuracy of R_s. The major sources of errors may be the nonlinearity of HTS and the RF leakage at the low frequency end, and the deficiency in treating coupling and bends at high frequencies. The temperature-dependence measurement shows that the fractional shift of the resonant frequency is independent of frequency. This confirms that the penetration depth of the superconductor is frequency-independent. The nonlinearity of the superconductor is also observed as the circulating power increases, in terms of skewed resonant peaks and reduced quality factors.

10.3 Future work

(1) So far, the drive to use the CBCPW in a microwave circuit was mainly its mechanical strength with the ease of mounting on a metal surface. Some research interests were also focused on the parasitic microstrip mode. But there has not been much attention to the effect of conductor backing on the slotline mode. From the information gathered in this work, it is worthy of further investigation on the origin of the immunity to spurious modes for the CBCPW delay line. If this effect can be used in a wider application background, it would be of more importance as this may provide an alternative technique to the troublesome wire-bonding in coplanar circuits.

(2) To improve the measurement accuracy, more sophisticated calibration process for the low-temperature measurement may be required. A TRL low-temperature calibration set should be beneficial to achieve a more accurate and wideband calibration. The poor signal-to-noise ratio at the low frequency end of the resonance measurement affects the accuracy in characterising the HTS materials. This would have been improved if the external coupling could be increased. But the effect of the therefore increased circulating power should also be carefully considered.

(3) For the resonant measurements with -10dBm input power, although the circulating power is believed to be very low, the measured results still show certain consistency with the nonlinearity. To justify the nonlinear region, measurements with lower than -10dBm input power are needed. But an output amplifier may have to used, as the signal-to-noise ratio at the low frequency end are expected to be too low for direct measurements.

(4) The match of the delay lines can be further optimised. This not only involves the input port match, but also the match between a straight line and a meander line, and the match

of a meander line with the spiralling structure. Generally speaking, it is about the match with a structure, the impedance of which is affected by the presence of mutual coupling.

(5) All the available loss formulas for the coplanar waveguide are derived assuming a straight transmission line. So there are some limitations in applying these formulas to a meander line with mutual coupling and bend structures. The conformal mapping method may be useful to establish the current distribution in the coupled coplanar lines and investigate the effect of coupling on the conductor loss.